EUROPEAN MECHANICAL SCIENCE

2017

VOLUME
01

ISSUE
01

Editors: M. Özcanlı, H. Serin

Editorial Board

European Mechanical Science 2017, Vol. 1(2): I-I
Original Paper

Contents

European Mechanical Science 2017, Vol. 1(1): 1-8
Original Paper

Non-Destructive examination of underground pressure vessels using acoustic emission (AE) techniques§

Deniz Karaduman[1], Durmuş Ali Bircan[2], Ahmet Çetin[3]

[1,2,3]Çukurova University, Department of Mechanical Engineering, 01330 Balcalı, Adana, TURKEY

Abstract

The methodology of Acoustic Emission (AE) for detecting and monitoring damages, cracks and leaks in different structures is widely used and has earned a reputation recently as one of the most reliable and well-established technique in Non-Destructive Testing (NDT). Besides evaluation of fracture behavior, crack propagation and fatigue detection in metals, composites, wood, fiberglass, ceramics and plastics; it can also be used for detecting faults and pressure leaks in pressure vessels, tanks and pipes.

As a relatively "clean" form of energy, Liquefied Petroleum Gas (LPG) is widely used for industrial applications and domestic heating. Periodic inspection of buried tanks used for LPG storage is complicated and limited because of their underground location. This situation prevents "conventional" NDT techniques from being used. So, AE testing which fulfills all safety requirements, is the most appropriate and cost-effective technique that can be used for periodic inspection and proof testing.

In addition of a general presentation on the AE technology and its applications, this study provides comprehensive evaluation of AE testing techniques of underground LPG tanks during service in accordance with TS EN standards. Some representative results and data obtained from a performed AE test are also provided.

Keywords: Acoustic Emission (AE), Non-Destructive Testing (NDT), Underground LPG Tanks, In-Service Monitoring.

1. INTRODUCTION

Acoustic Emission (AE) is defined as a phenomenon, where one or more local sources in materials, which are under stress, are emitting energy and producing temporary elastic waves. AE covers a broad range in material science, construction and process development. The largest events which can be analyzed by AE are seismic occurrences, the smallest are dislocations occurring in metals by load. Between these two, there is a broad range of detailed research work and industrial application [1]. One of those application area is the inspection of buried LPG tanks of industrial plants and some domestic buildings.

AE Testing (AET) has become a recognized NDT method commonly used to detect and locate faults in mechanically loaded structures and components. AE can provide comprehensive information on the origination of a discontinuity (flaw) in a stressed component and also provides information pertaining to the development of this flaw as the component is subjected to continuous or repetitive stress [2].

Huge quantities of LPG tanks have been installed in Turkey during the last decade. For the vast majority of those tanks are located under the ground because of the safety considerations. Since inspection is obligated by national legislations of occupational health and safety, after ten years of operation huge numbers of tanks are now set for inspection. Traditional methods of inspection require that the tank is unearthed, which means that they are cumbersome, slow and expensive, i.e. very cost-ineffective [2]. Thus, NDT techniques of AE are preferred for periodic inspection and proof testing of those tanks.

This procedure is currently being validated via experimental tests on a large number of LPG tanks by comparing the results with those obtained by conventional NDT techniques. Initial results appear to confirm the effectiveness of the technique and encourage further research in this field [3].

The European Standards TS EN 12817 [4] (comprised of LPG Tanks up to 13 m^3), TS EN 12819 [5] (comprised of LPG Tanks greater than 13 m^3) and TS EN 14584 [6] allows AE-based techniques to be used in periodic inspection and the requalification of underground LPG tanks. The main objective of this study was to present general information

*Corresponding authour
Email: ahmetcetin@cu.edu.tr (A. Çetin)
§ This paper was presented at the IMSEC-2016

about AE technology and its applications, to provide comprehensive analysis of AE testing techniques of underground LPG tanks during service and to review the results and the outcoming data obtained from a performed AE inspection of an underground LPG tank belonging to a domestic building with a capacity of 5 m^3.

2. OVERWIEV ON AE TESTING TECHNIQUE

2.1 Principles of AE Testing

AE testing refers to a technique of testing, recording and analyzing AE signals using apparatus as well as speculating on the status of an AE source as normal or not based on AE signals. The elastic waves sent from the AE source are transmitted to the material surface via a transmission media and converted to electric signals by sensors before being magnified, processed and recorded. Through the analysis and processing of acquired signals, any defects inside the material could be detected [7] as illustrated in Figure 1.

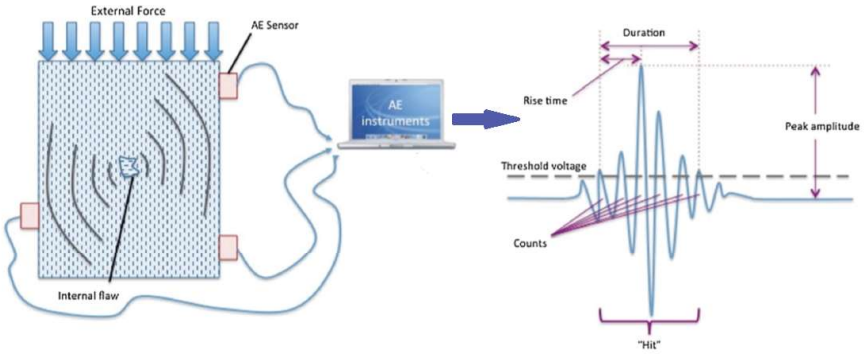

Figure 1: Principle of AET. [8]

The diagram illustrates various parameter defined below:

- Count: The number of times a peak in the wave lies above a set threshold frequency.
- Hit/Event: A collective term for a group of AE counts that lie above the threshold amplitude. A hit is also defined as a signal that triggers the system channel to accumulate data.
- Rise time: The time between a wave triggering above the threshold amplitude and the time of the peak amplitude of that wave. The rise time is related to the source-time function and can describe the type of fracture or eliminate noise signals.
- Duration: The time between an AE waveform triggering above the threshold and its disappearance below that threshold. The duration is related to the source magnitude and noise filtering.
- Amplitude: The peak voltage of a waveform. It is closely related to the magnitude of the source event [8].
- MARSE (Measured Area Under the Rectified Signal Envelope): It is derived from the rectified voltage signal over the duration of the AE waveform with voltage-time units and it is strongly sensitive to amplitude and duration [9].

The technology involves the use of ultrasonic sensors (20 Khz-1 Mhz) that listen for the sounds of material and structural failure. AE frequencies are usually in the range of 150–300 kHz, which is above the frequency of audible sound. Crack growth due to hydrogen embrittlement, fatigue, stress corrosion, and creep can be detected and located with the use of this technology. High-pressure leaks can also be detected and isolated [2].

When considering detecting an AE waveform, one must decide on the type of sensor, pre-amplification and band-pass filters. Typical sensors used in AET are piezoelectric in nature, which convert mechanical strain of the piezo element into an electric signal [10]. Another important consideration is how to attach the sensor to the material as well as the location of multiple sensors.

AE signals are very weak and must be amplified around 100 times in order to allow detection. Finally, to reduce background noise from interfering with AE signal interpretation, a band-pass filter is included into the system. Calibration of the system can be achieved in several ways; however, the commonest is the use of Hsu-Nielsen method as known as

Pencil Lead Break (PLB) tests [11]. Components of a typical AE instruments are illustrated schematically in Figure 2.

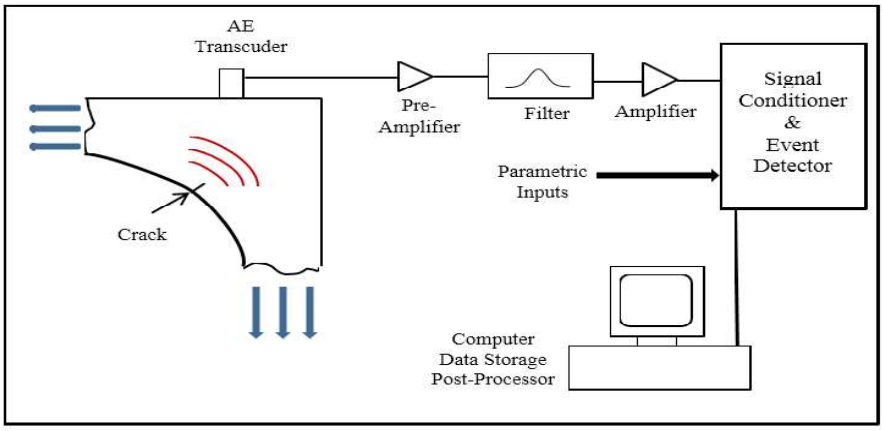

Figure 2: A typical AE system setup [12]

2.2 Applications of AE Testing

As laboratory work; it's a very effective instrument in the field of material examining and observation of deformation and fracture behavior. During the manufacturing process; it's used in appearance design phase like thermos-compression bonding and shaft straightening, observation of welding and wood drying process and corrosion testing. As a structural inspection method; it's very satisfactory about determination of flaw, crack, leakage, corrosion and welding failure in pressure vessels, storage tanks, pipelines, airplane and airspace vehicles, bridges, railways, etc. Besides of those determinations, AE techniques can localize the failure area. AET applications of pressure vessels, pipelines, storage tanks and bridges are illustrated in Figure 3.

Figure 3: Examples for AET application [13, 14, 15, and 16].

3. EXPERIMENTAL SET-UP

3.1 Installation of Testing Equipment

On-site inspection has been performed using a mobile laboratory, equipped with a LPG pressurization device, MISTRAS Micro-II Digital AE System processor and other instruments for AE testing. Tests have been performed on a tank designed and manufactured to operate in an underground location with "horizontal" position. The storage tank with a capacity of 5 m^3 has a cylindrical geometry (1200mm outer diameter, 7mm shell thickness and 4050 mm length) and is closed by hemispherical ends at both sides. The operating temperature is between -10°/+40°C and operating pressure is 15 bar. Real time pressure measurements have been performed using a manometer shown in Figure 4 (ECO1 Di-

gital Ex-proof Manometer) directly connected to the gas pipeline near the tank. Because of the limited accessible area and the presence of components (valves, pipes and other accessories), only two piezoelectric sensors shown in Figure 4 (KRNI150 100kHz-400kHz) could be positioned on the tank surface by using magnetic connection apparatus, with a mutual distance of 400mm, shorter than determined maximum allowed sensor spacing according to TS 11634 [18] and TS 15495 [19].

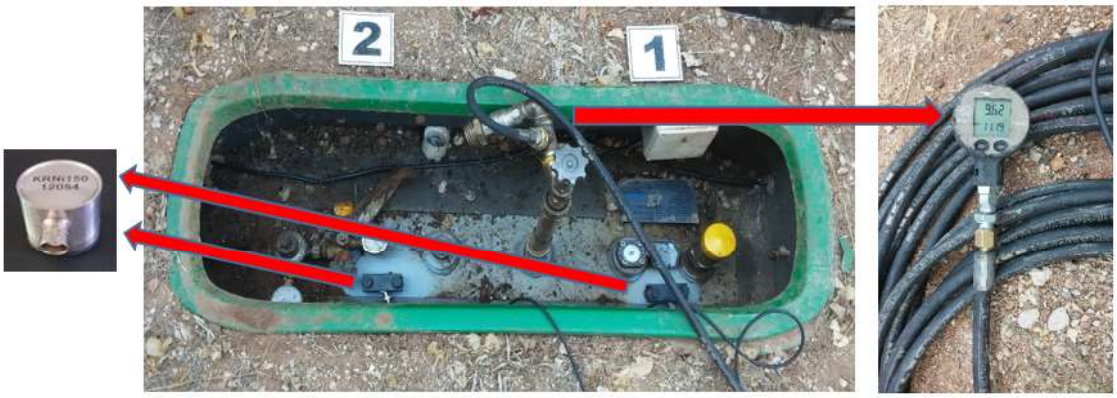

Figure 4: AE sensor mounted on the tank surface and manometer connected to the gas pipeline.

Sensors, cables and preamplifiers have all been successfully tested for compliance with existing standard requirements [20-22]. Calibrations of the piezoelectric sensors are performed by using "Hsu-Nielsen" method as known as PLB method. This procedure is very crucial in order to define the senility of the sensors. Any inaccuracy of the coupling of the sensors could lead to obtain faulty data. "Hsu-Nielsen" method is shown in Figure 5 both schematically and visually.

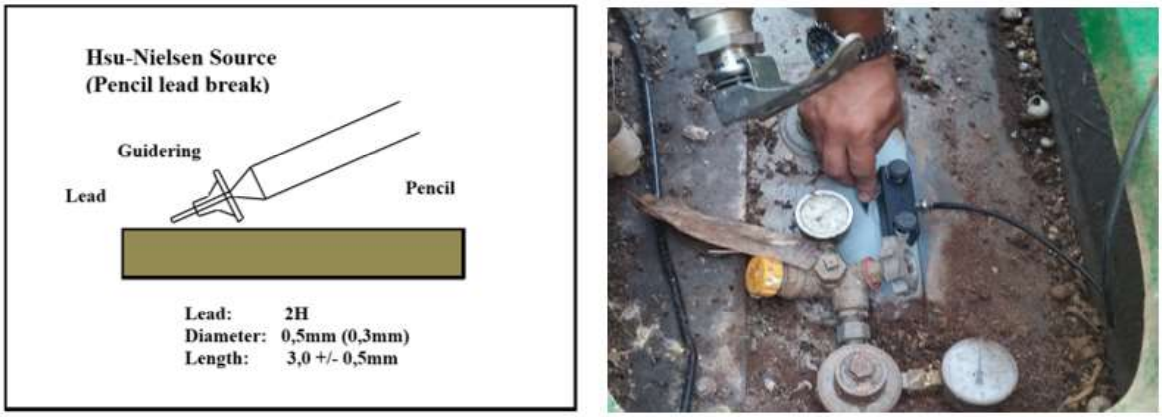

Figure 4: Illustrations of Hsu-Nielsen method (PLB).

After detecting the background noise value (dB_{AE}), threshold value is set to 45 dB_{AE} to avoid environmental ambiguities. Calculation of evaluation threshold is shown in Figure 5 and in Table 2.

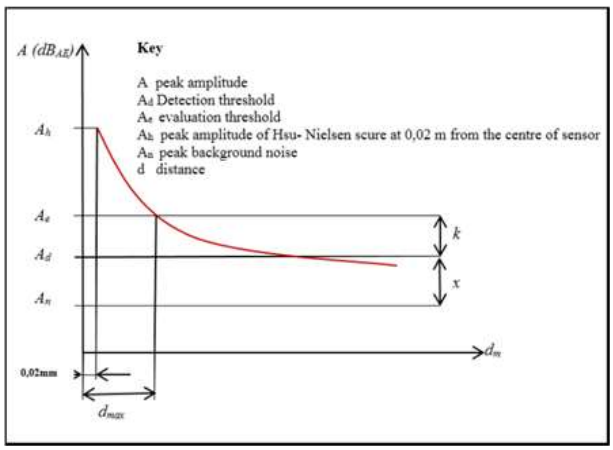

Figure 5: Determination of the maximum sensor spacing from attenuation curve. [6]

Table 2. Calculation of evaluation threshold.

Key		dB_{AE}
A_n	Peak background noise	21
A_d	Detection threshold (A_n+X; X=12 dB)	33
A_e	Evaluation threshold (A_d+K;K=12 dB)	45

3.2 Pressurization and Data Acquisition

The pressure equipment was monitored prior to pressurization for 10 min at the detection threshold, to confirm that there is no ambient noise, which might interfere with the test. To avoid noises caused by turbulence, as recommended by existing standard procedures [23], the pressurization device has allowed a pressure gradient ≈ 0.3 bar/min to be held throughout the test.

When reached at the desired pressure level, it's waited at least 5 min at every pressure grade. At the top pressure level, pressurization has been stopped and stabilized at least 10 min. During these process, LPG is used as the pressurization item. Pressure sequence and loading is calculated as the %50, %85 and %110 capacity of tank operation pressure. At every stage of desired pressurization, storage tank was monitored by sensors with a period of 5 min. The sequence of pressurization of this tank was shown in Figure 6.

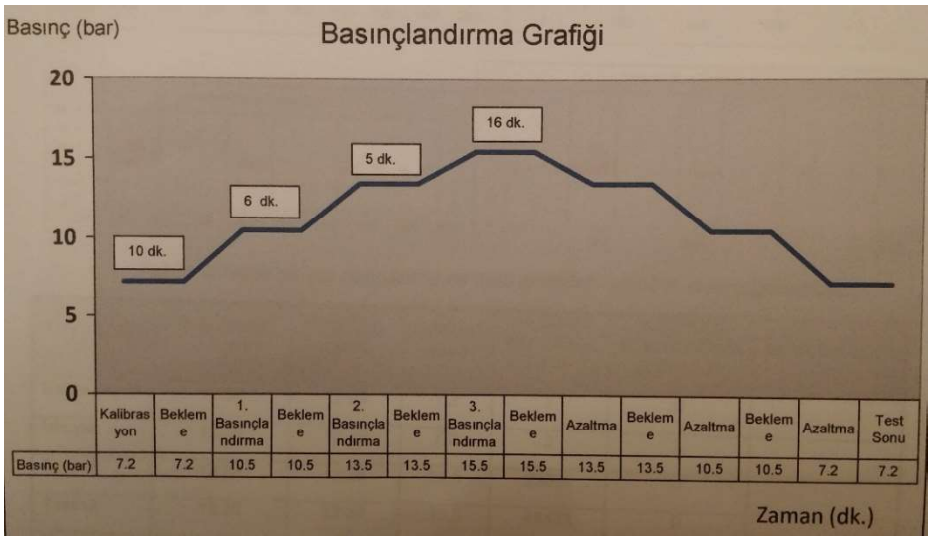

Figure 6: The sequence of pressurization of the tank.

3.3 Data Acquisition

Data acquisition and processing is performed using MISTRAS Micro-II Digital AE System with "AEwin for SAMOS" software packet. Data graphs of testing obtained via AE system and test parameters were illustrated in Figure 7 and Table 3.

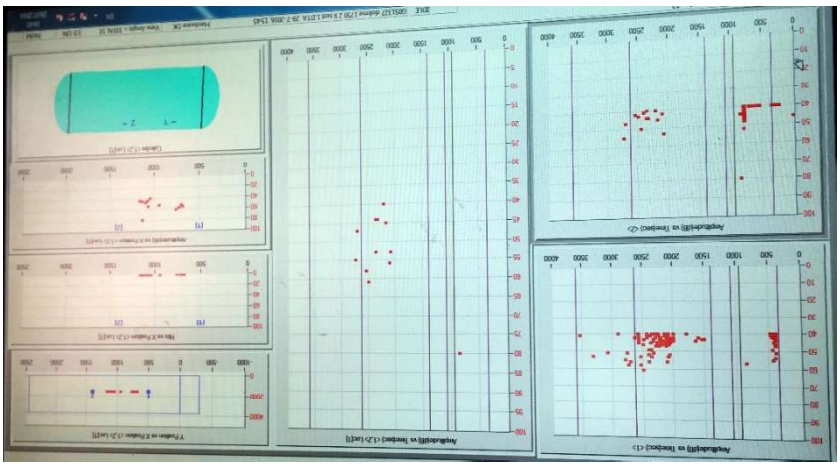

Figure 7: Verification and data graphs of the test (Screen View).

Table 3. Test Parameters.

Test Step	Start Time	Finish Time	Pressure (Bar)	AE Hits (Total)	AE Events (Total)
Calibration	15:41	15:43	9,85	64	1
Background Noise Observation	15:43	15:53	9,85	27	0
1st Pressurization	15:53	16:08	11	866	1
Test	16:08	16:13	11	866	1
2nd Pressurization	16:13	16:34	15,5	960	10
Test	16:34	16:49	15,5	970	12

4. INTERPRETATIONS OF TESTING RESULTS

4.1 Grading Criteria and Real-time Control

The grading criteria are used for real time control and for subsequent source severity classification. They shall be defined by the AE test organisation on the basis of experience. Real-time control parameters are given in Table 4 below.

Table 4. Example of definition of real-time control parameters [6].

Real-time Control Parameters	Values
EB	1000
A1	105 dB_{AE}
N1	5
AC1	100 dB_{AE}
NC1	5
AC2	88 dB_{AE}
NC2	20
N3	2
Z	0,1 $d_{max,u}$
t_h	5 min

The values in the table are an example only and under no circumstances should these example values be used. Grading criterias are;

- the number N1 of located burst signals with a distance corrected peak amplitude above a “high” specified value A1;

- the occurrence of a number N3 of located burst signals above the specified corrected peak amplitude AC2 in a defined time period “t_h” during the hold. The time period “t_h” starts 2 min after the beginning of the hold period.

- the number NC1 of located burst signals with a distance corrected peak amplitude above a “high cluster” specified value AC1 within a square of an edge length or circle with a diameter of Z.

- the number NC2 of located burst signals with a distance corrected peak amplitude above a “low cluster” specified value AC2 within a square of an edge length or circle with a diameter of Z [6].

4.2 AE Source Location Cluster Severity Grading and Test Results

The AE source location clusters shall be graded according to their AE activity and intensity into 3 grades (see Table 5) based upon EN 13554 [20].

Table 5. Source severity grading [20].

Source severity grading	Definition	Further actions
1	minor source	no further actions shall be necessary; included in the report for comparison with subsequent tests
2	active source	further NDT shall be recommended if the source is associated with specific parts of the pressure equipment (e.g. weld seams, attachments, etc.)
3	very active source	Further evaluation by other appropriate NDT shall be carried out before the pressure equipment goes into service

The real-time control parameters and the grading of the tank subjected to AET are shown in Table 6 below. During the test 12 AE event has been detected. 11 of those detections are between 40-60 dB_{AE} range. Only one detected AE event (maximum detection) with a value of 80 dB_{AE} is also below the values of A1, AC1 and AC2. Thus, the LPG tank subjected to AET is graded as "Class-1" with minor source.

Table 6. Tank Classification.

Maximum Event Frequency	12		Standard Value	Measured Value	Tank Class
		N1	5	0	CLASS-1
		NC1	5	0	
		NC2	20	0	
		N3	2	0	

5. CONCLUSION

An AE-based inspection of underground LPG tanks has been proposed to perform quick and cost-effective experiments. But in some cases, experimental set-up should have some limitations due to small and crowded accessible area on the tank. In this examination, only two sensors was used. Despite of those limitations, AE based inspection of the tank has been performed successfully. This method also increases the safety of the operators involved in the test and protects natural resources and the environment (no disposal of residuals necessary, no cleaning and no draining of contaminated water, etc.).

As a result, inspections based on AE proves to a technologically advanced and reliable technique that reduces downtime and inspection costs of the tank. Additionally, the method illustrated in this study has a potential and widely applicable field for other industrial instruments and furthermore studies could be prompted.

6. ACKNOWLEDGEMENTS

This study is supported by Çukurova University Research Fund [FYL-2016-6515].

REFERENCES

[1] Tuncel S., (2008), "Latest Developments in The Field of NDT Technologies: Acoustic Emission", 3rd International Non-Destructive Testing" Symposium and Exhibition, Istanbul Turkey, April 2008.

[2] Hellier C. J., (2003), "Handbook of Nondestructive Evaluation", vol.70, pp.466-470.

[3] Petrisa C. D., Siteb C.D., Lenzunic P., Mazzocchib V., Mennutia C., (2004), "An Innovative AE Technique For The Verification of Underground and Buried Pressure Equipment", ICEM12- 12th International Conference on Experimental Mechanics, Politecnico di Bari, Italy

[4] Turkish Standard TS EN 12817, (2010), "LPG Equipment and Accessories - Inspection and Requalification of LPG tanks up to and including 13 m^3", ICS 23.020.30.

[5] Turkish Standard TS EN 12819, (2009), "LPG equipment and accessories - Inspection and requalification of LPG tanks greater than 13 m^3", ICS 23.020.30.

[6] Turkish Standard TS EN 14584, (2013), "Non-destructive testing - Acoustic emission testing- Examination of metallic pressure equipment during proof testing - Planar location of AE sources", ICS 17.140.20&77.040.20.

[7] Gao L., Zai F., Su F., Wang H., Chen P. and Liu L. (2011), "Study and Application of Acoustic Emission Testing in Fault Diagnosis of Low-Speed Heavy-Duty Gears", Sensors (Basel). 11(1), pp.599-611.

[8] Rashid M.S. and Pullin R., (2014), "The Sound of Orthopaedic Surgery - The Application of Acoustic Emission Technology in Orthopaedic Surgery: A Review", Eur J. Orthop. Surg. Traumatol 24:1–6.

[9] Safari A., (2006), "Acoustic Emission Analysis of the Effect of a 2D Wedge Shaped Blade on the Compact Bone Cutting Process", Department of Mechanical and Electronic Engineering School of Engineering Institute of Technology Sligo.

[10] Muravin B (2009), "Acoustic Emission Science and Technology", J Build Infrastruct Eng Israeli Assoc. Eng. Archit Israel.

[11] Nielson A (1980), "Acoustic Emission Source Based on Pencil Lead Breaking", Report 80-15, Danish Welding Institute.

[12] Huang M.,Jiang L., Liaw P.K., Brooks C.R., Seeley R., and Klarstrom D.L., (2009)," Using Acoustic Emission in Fatigue and Fracture", Materials Research, Nondestructive Evaluation: Overview, University of Tennessee.

[13] Federal Institute for Materials Research and Testing (2008), "Evaluation of Composite Cylinders Using Acoustic Emission", Hydrogen Storage Systems for Automotive Application. Acoustic

[14] Emission Instrumentations, http://iti.northwestern.edu.

[15] Akustik Emisyon, http://www.tr-tuv.com.tr.

[16] McCormick R.R., (2007), "Advancements In Acoustic Emission Testing Of Steel Highway Bridges", Report, Infrastructure Technology Institute, School of Engineering and Applied Science, Northwestern University.

[17] Gholizadeh S., Leman Z. and Baharudin B.T.H.T, (2015), "A Review of The Application of Acoustic Emission Technique in Engineering", Structural Engineering and Mechanics, Vol. 54, No. 6, pp. 1075-1095.

[18] Turkish Standard TS 11634, (1995), "Nondestructive Testing-Guidelines for mounting Piezoelectric Acoustic Emission Sensors", ICS 77.040.20.100.

[19] Turkish Standard TS EN 15495, (2008), "Non-destructive testing-Acoustic emission- Examination of metallic pressure equipment during proof testing Zone location of AE sources".

[20] European Standard EN 13554, (2011), "Non-destructive testing - Acoustic emission - General principles", ICS 19.100.

[21] European Standard EN 13477-1, (2004), "Non-destructive testing - Acoustic emission- Equipment characterization- Part 1: Equipment description", ICS 19.100.

[22] European Standard EN 13477-2, (2010), "Non-destructive testing-Acoustic emission - Equipment characterization- Part 2: Verification of operating characteristic", ICS 19.100.

[23] ISO/DIS 16148.2, "Gas cylinders- Refillable seamless steel gas cylinders-Acoustic emission examination (AEE) for periodic inspection".

European Mechanical Science 2017, Vol. 1(1): 9-14
Original Paper

Analysis of dehumidification and humidity removal process of desiccant wheel§

Osman Kara[1], Ertaç Hürdoğan[2], Orhan Büyükalaca[3]

[1,2,3]Energy System Engineering/ Osmaniye Korkut Ata University, Turkey

Abstract

Desiccant cooling technology is an environmentally attractive alternative to conventional mechanical air conditioning. A desiccant cooling system is a suitable way to improve indoor air quality due to its superior humidity control and it also provide as economical and cleaner for hot and humid regions. The most important component of the technology is the desiccant wheel which is used to remove the humidity of air. In this study, the analysis of dehumidification and humidity removal process of desiccant wheel were carried out using the performance data given by manufactures of the desiccant rotary wheel. Two parameters (F_d, F_r) were defined for the analysis of the process. It was found that dehumidification and regeneration processes do not occur at constant wet bulb temperature. An equation for F_d and F_r which depends on the humidity ratio of outdoor air and regeneration temperature was composed.

Keywords: Air conditioning, Desiccant cooling, Dehumidification, Desiccant wheel,

1. INTRODUCTION

Desiccant cooling consists in dehumidifying the incoming air stream by forcing it through a desiccant material and then drying the air to the desired indoor temperature. To make the system working continually, water vapour adsorbed/absorbed must be driven out of the desiccant material (regeneration) so that it can be dried enough to adsorb water vapour in the next cycle. This is done by heating the material desiccant to its temperature of regeneration which is dependent upon the nature of the desiccant used. A desiccant cooling system, therefore, comprises principally three components, respectively, the regeneration heat source, the dehumidifier (desiccant material), and the cooling unit [1].

The purpose of a solid desiccant cycle is to reduce the moisture content of the ambient fresh air. A typical approach for using solid desiccants for dehumidifying air streams is to impregnate them into a light-weight honeycomb or corrugated matrix that is formed into a wheel. The wheel is usually divided into two sections. The process air flows through one section of the wheel to be dehumidified, while a reactivation airstream passes through the other section to regenerate the wheel. The desiccant wheel rotates slowly between the process and the regeneration airstreams in order to make the process continuous [2].

The solid desiccants are used in different technological arrangements. One of the typical arrangements consists of a slowly rotating wheel impregnated with a desiccant like a silica gel or a molecular sieve, in which a part of the wheel is intercepting the incoming air stream while the rest of it is being regenerated. For continuous operations, adsorption and regeneration must be performed periodically. Solid desiccants are compact, less subject to corrosion and carryover, hence in comparison with the other methods, desiccant wheels are more common [3]. Many researches carried out a lot of studies for design, modeling and optimization of solid desiccant cooling. Jia et al. [4] improved desiccant wheel adsorption efficiency about 50% by preparation of a new kind of hybrid desiccant (silica gel and lithium chloride). They investigated on the effect of a new adsorbent on desiccant cooling system and achieved 35% efficiency increase to the silica gel [5].

Antonellis et al. investigated the use of a desiccant wheel for air humidification with a numerical and experimental approach. It is shown that the system can properly provide an air stream at satisfactory humidity ratio through an appropriate arrangement of the desiccant wheel. When the ratio process air flow rate to the regeneration air flow rate is greater than 1.3, the desired outlet humidity can be achieved. Besides the lower the outdoor air temperature, the higher the process air flow rate [6].

Two-stage desiccant wheel systems are an effective way to improve the dehumidification performance. Liu et al. compared the performances of a one-stage system and a two-stage system with identical heat transfer areas, with required

*Corresponding authour
Email: ehurdogan@osmaniye.edu.tr (E. Hürdoğan)
§ This paper was presented at the IMSEC-2016

heating source temperature. Compared to the one-stage system, the regeneration temperature of the two-stage system is lower [7].

In this study, the analysis of dehumidification and humidity removal process of desiccant wheel were carried out. In the analysis, the performance data given by manufactures of the desiccant rotary wheel was used. The effect of relevant parameters such as inlet air humidity, regeneration temperature, air mass flow rate, etc., on performance of desiccant wheel was discussed.

2. MATERIAL AND METHOD

The most important component of dehumidification air conditioning system is desiccant wheel. Some of the publications and introduction brochures related with the dehumidification regenerators point out that dehumidification and removal of humidity processes (regeneration, reactivation) realize approximately at constant enthalpy (approximately at constant wet bulb temperature) [4,9].

Dehumidification and removal of humidity processes are represented with the curves (A→B) and (C→D) in Figure 1. However, dehumidification and regeneration processes do not occur at constant wet bulb temperature according to the data given by the rotary desiccant wheel manufactures. Actual increase in dry bulb temperature during dehumidification (A→B') is higher than that of the constant wet bulb case (A→B). This is due to fact that a chemical thermal energy arises and the energy carried by the matrix of the wheel dehumidification regenerator from the regeneration air, which is hotter from the process air [8]. Because of this additional energy, dry bulb temperature further increases. The ratio of additional dry bulb temperature increase ($t_{B'}$-t_B) to total dry bulb temperature increase ($t_{B'}$-t_A) was defined as:

$$F_d = \frac{t_B - t_B}{t_B - t_A} \tag{1}$$

Similarly, dry bulb temperature decrease higher than constant wet bulb temperature case during regeneration (C→D'), due to sensible heat transfer to the process air. The ratio of additional dry bulb temperature decrease ($t_{D'}$-t_D) to total dry bulb temperature decrease ($t_{D'}$-t_C) was also defined as:

$$F_r = \frac{t_D - t_D}{t_D - t_C} \tag{2}$$

It is important to determine the values of F_d and F_r accurately to able to analysis the desiccant cooling systems. In this study the performance data given by manufactures of the desiccant rotary wheel was used to calculate F_d and F_r. Analysis of the data released that F_d and F_r are functions of dry bulb temperature and humidity ratio of the dehumidified (process) air and the regeneration air.

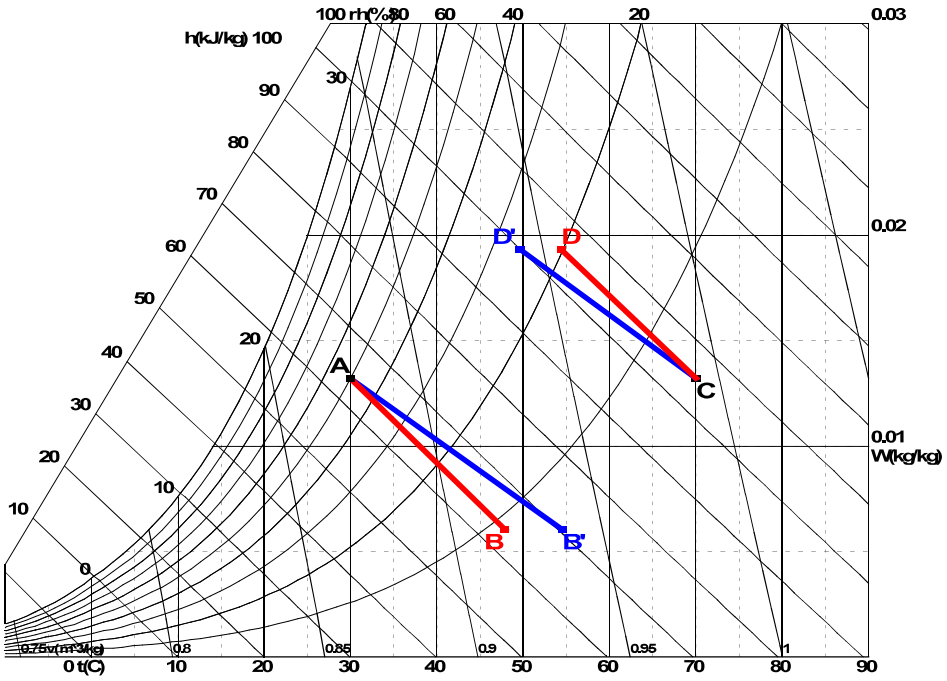

Figure 1. The process of dehumidification (A-B) and removal of humidity (C-D)

3. RESULTS ANS DISCUSSION

In this study; the humidity ratio of the process air and the regeneration air are equal, since the same outdoor air was used as the process air and the regeneration air. Figure 2 shows the variation of F_d values with the humidity ratio (W) of the outdoor air for a 70 °C regeneration air temperature ($T_{reg.temp.}$). In the figure, F_d values are plotted for different outdoor air dry bulb temperatures varying between 25 °C and 40 °C. As can be seen from the figure, F_d decreases smoothly with increasing humidity ratio of outdoor air and dry bulb temperature of the outdoor air has no significant influence on F_d. Similar results were obtained for different regeneration air temperatures.

Figure 3 shows the variation of F_r values with the humidity ratio of the outdoor air for a 70 °C regeneration air temperature at different outdoor air dry bulb temperatures. As can be seen from the figure, results similar to with F_d were obtained for F_r.

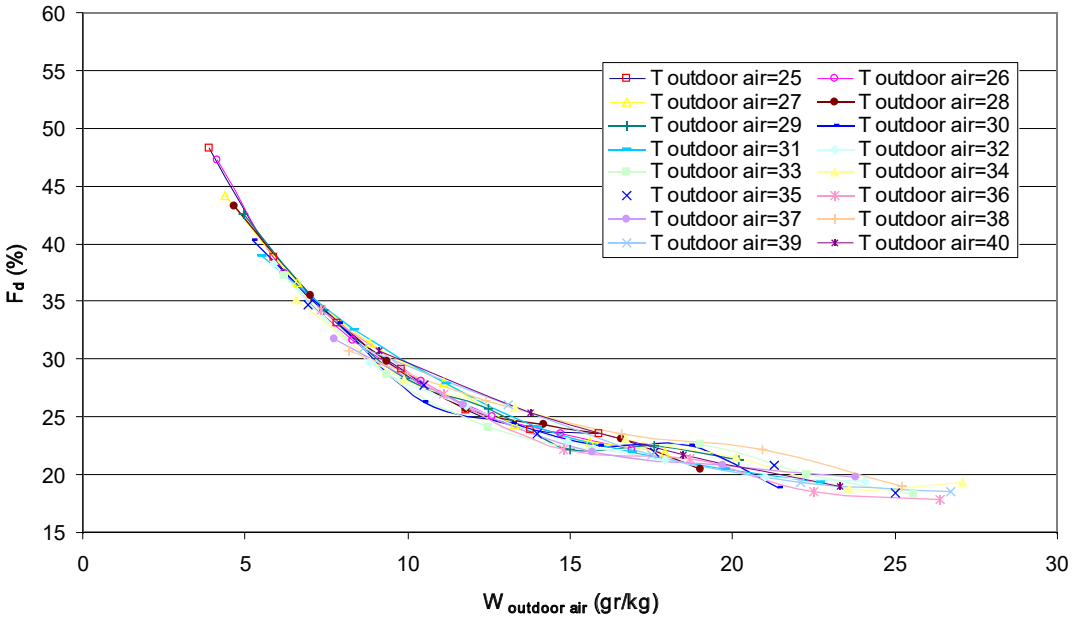

Figure 2. Variation of F_d at 70 °C regeneration air temperature with humidity ratio of the outdoor air for different outdoor air temperatures

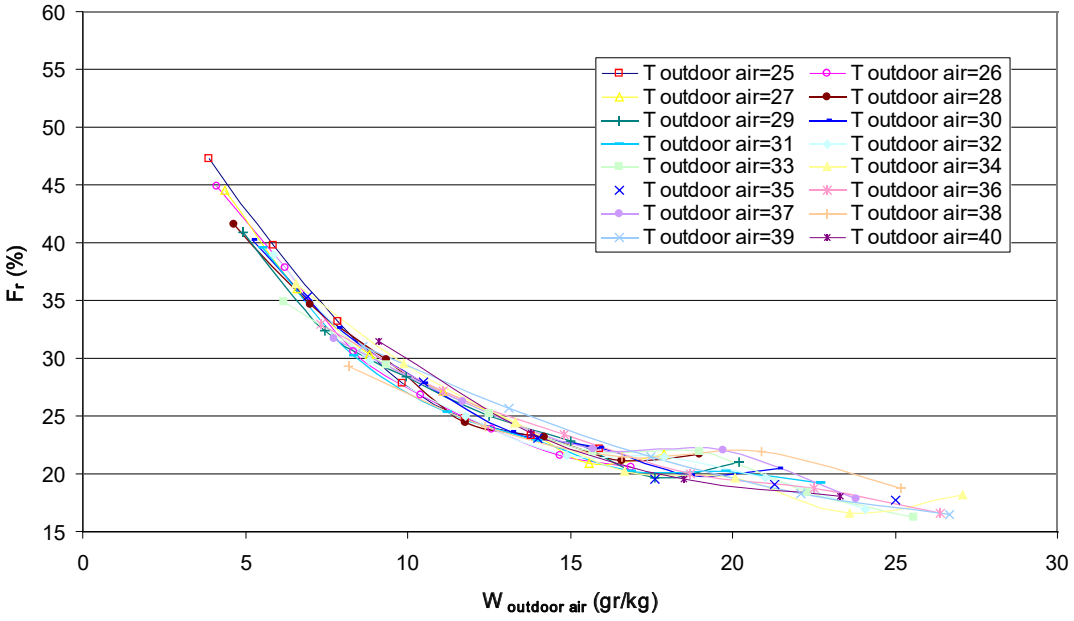

Figure 3. Variation of F_r at 70 °C regeneration air temperature with humidity ratio of the outdoor air for different outdoor air temperatures

Figure 4 shows values of F_d and F_r, which were calculated for different regeneration air temperatures for dehumidification and humidity removal processes. As it can be seen from the Figure, F_d and F_r are almost the same for a given regenera-

tion temperature. Therefore, the dehumidification and humidity removal data were handled together in order to obtain equations required for the system analysis. Figure 5 shows the values of F_d and F_r, which were obtained at different regeneration air temperatures. The curves which were fitted (by using least square method) to the calculated data for each regeneration temperature were also shown in the figure.

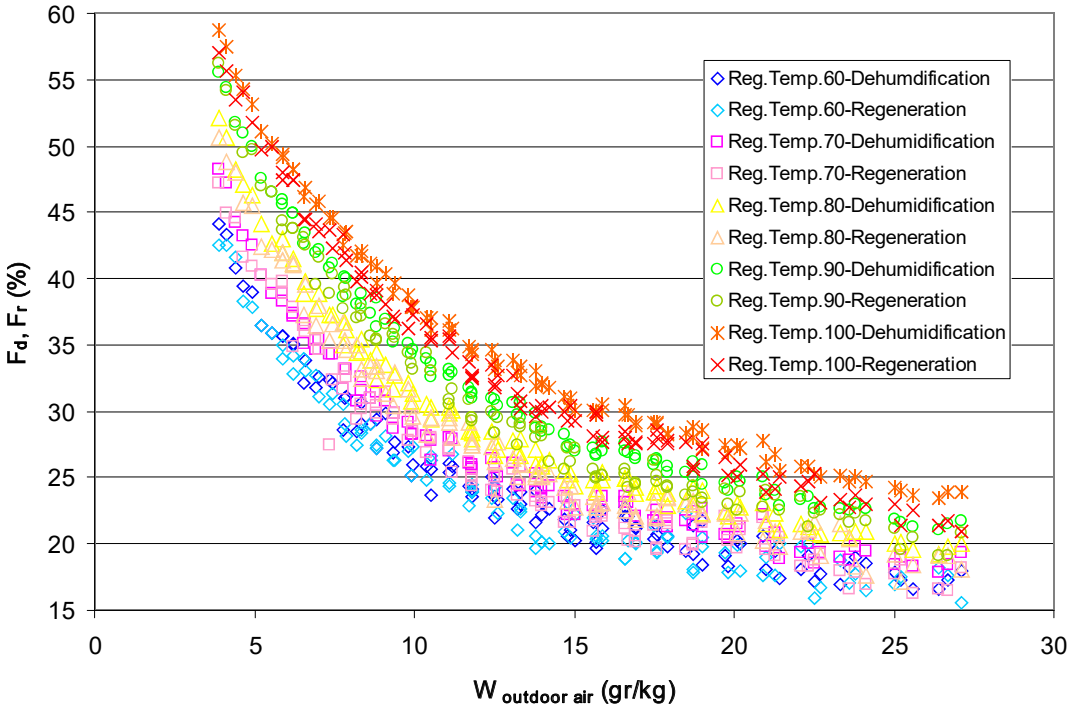

Figure 4. The values of F_d and F_r which were calculated at different regeneration air temperature for dehumidification and humidity removal processes

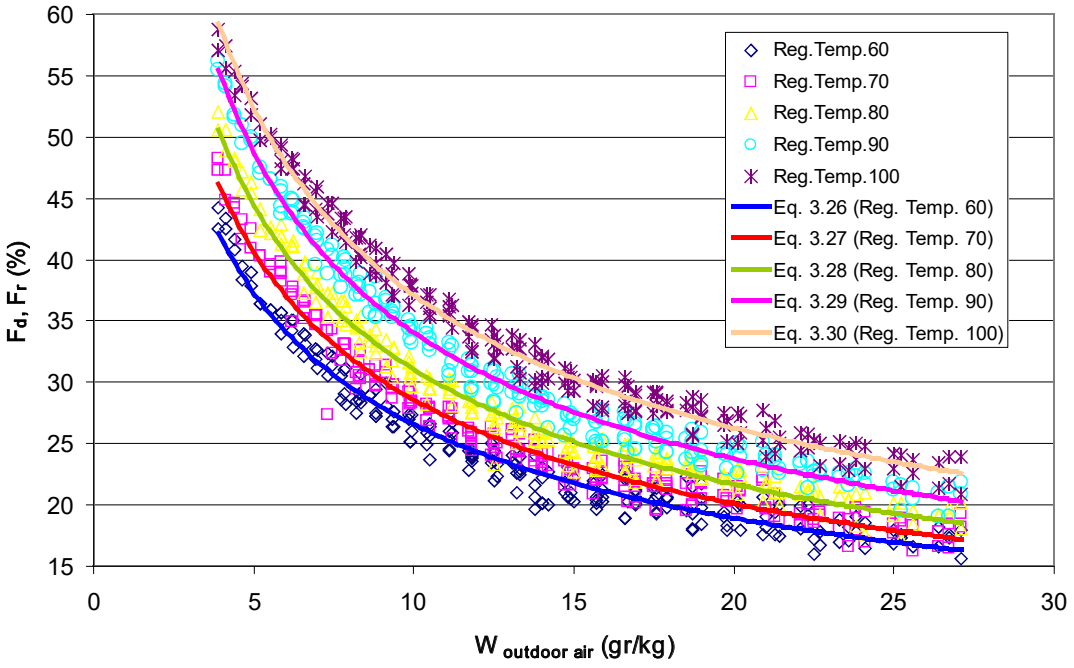

Figure 5. The values of F_d and F_r, which were obtained at different regeneration air temperature, related with the humidity ratio of the outdoor air (Equations 3-7).

The equations of the curves which were fitted to the calculated data for each regeneration temperature were listed below:

$$T_{reg.\ temp.} = 60\ ^{o}C: \quad F_d = F_r = 82.136 \times W^{-0.4901} \qquad (R^2=0.957) \qquad (3)$$

$$T_{reg.\ temp.} = 70\ ^{o}C: \quad F_d = F_r = 92.289 \times W^{-0.509} \qquad (R^2=0.970) \tag{4}$$

$$T_{reg.\ temp.} = 80\ ^{o}C: \quad F_d = F_r = 102.45 \times W^{-0.518} \qquad (R^2=0.977) \tag{5}$$

$$T_{reg.\ temp.} = 90\ ^{o}C: \quad F_d = F_r = 112.41 \times W^{-0.5188} \qquad (R^2=0.983) \tag{6}$$

$$T_{reg.\ temp.} = 100\ ^{o}C: \quad F_d = F_r = 116.80 \times W^{-0.4979} \qquad (R^2=0.983) \tag{7}$$

Use of only one equation that is valid for all regeneration temperatures would be easier than use of separate equations for each regeneration temperature. In the next step of the study, possibility of representing all the data with only one equation was investigated. As a result, Equation 8 that includes influence of both humidity ratio of outdoor air and regeneration temperature was obtained:

$$F_d = F_r = 5.18 \times W^{-0.507} \times T_{reg.\ temp.}^{\ 0.652} \qquad (R^2=0.96) \tag{8}$$

Figure 6 shows the comparison of the values obtained from the curve and the real data. As seen from the figure, the equation follows the data successfully.

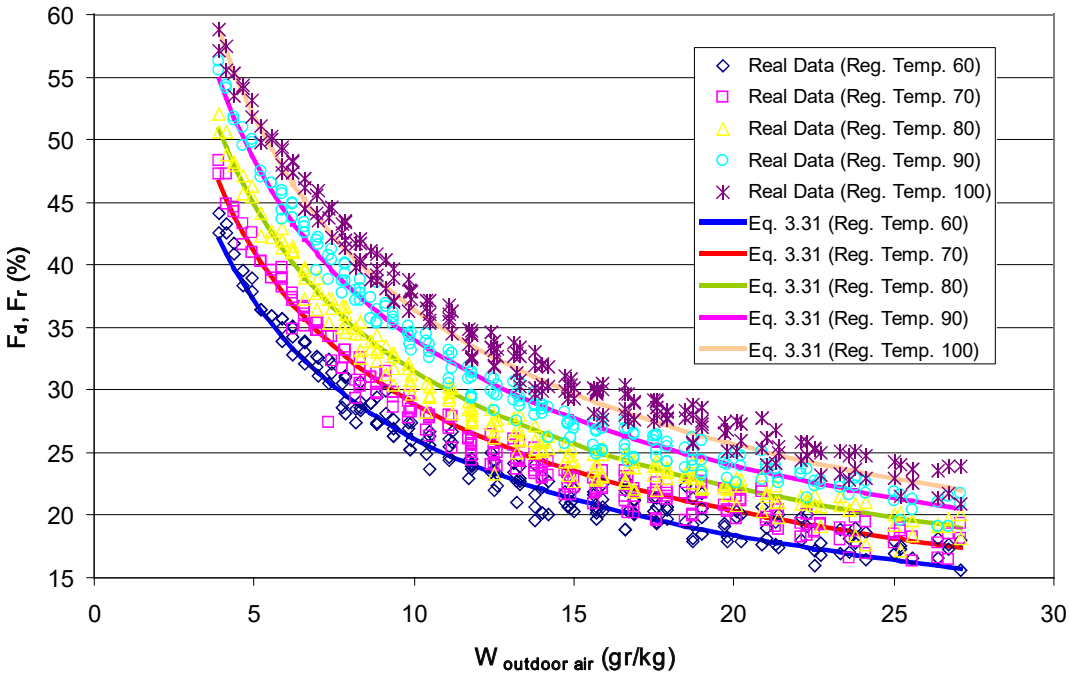

Figure 6. The values of F_d and F_r which were obtained at different regeneration air temperature related with the humidity ratio of the outdoor air (Equation 8).

4. CONCLUSION

In this study, the analysis of dehumidification and humidity removal process of desiccant wheel were carried out. The following main conclusions emerged from this study:

- Dehumidification and regeneration processes do not occur at constant wet bulb temperature according to the data given by the rotary desiccant wheel manufactures.
- Dry bulb temperature of the outdoor air has no significant influence on F_d and F_r.
- F_d and F_r are almost the same for a given regeneration temperature.
- An equation for F_d and F_r which depends on the humidity ratio of outdoor air and regeneration temperature was composed.

REFERENCES

[1] Daou, K., Wang, R., and Xia, Z. (2006). Desiccant cooling air conditioning: a review. Renewable and Sustainable Energy Reviews, vol. 10, no. 2, pp. 55-77.

[2] Al-Alili, A., Hwang, Y., and Radermacher, R. (2015). Performance of a desiccant wheel cycle utilizing new zeolite material: Experimental investigation. Energy, vol. 81, pp. 137-145. http://dx.doi.org/10.1016/j.energy.2014.11.084

[3] Ali Mandegari, M. and Pahlavanzadeh, H. (2009). Introduction of a new definition for effectiveness of desiccant wheels. Energy, vol. 34, no. 6, pp. 797-803. http://dx.doi.org/10.1016/j.energy.2009.03.001

[4] Jia, C.X., Dai, Y.J., Wu, J.Y., and Wang, R.Z. (2006). Experimental comparison of two honeycombed desiccant wheels fabricated with silica gel and composite desiccant material. Energy Conversion and Management, vol. 47, no. 15, pp. 2523-2534. http://dx.doi.org/10.1016/j.enconman.2005.10.034

[5] Jia, C.X., Dai, Y.J., Wu, J.Y., and Wang, R.Z. (2007). Use of compound desiccant to develop high performance desiccant cooling system. International Journal of Refrigeration, vol. 30, no. 2, pp. 345-353. http://dx.doi.org/10.1016/j.ijrefrig.2006.04.001

[6] De Antonellis, S., Intini, M., Joppolo, C.M., Molinaroli, L., and Romano, F. (2015). Desiccant wheels for air humidification: An experimental and numerical analysis. Energy Conversion and Management, vol. 106, pp. 355-364. http://dx.doi.org/10.1016/j.enconman.2015.09.034

[7] Liu, X.-H., Zhang, T., Zheng, Y.-W., and Tu, R. (2016). Performance investigation and exergy analysis of two-stage desiccant wheel systems. Renewable Energy, vol. 86, pp. 877-888. https://doi.org/10.1016/j.renene.2015.09.025

[8] ASHRAE (2004). Desiccant Dehumidification and Pressure Drying Equipment, American Society of Heating, Refrigeration and Air Conditioning Engineers, Vol.22, Atlanta.

[9] Kara O. (2009). Design of Air-Conditioning System with Dehumidification. Çukurova University Institute of Natural and Applied Sciences, Department of Mechanical Engineering.

European Mechanical Science 2017, Vol. 1(1): 15-23
Original Paper

Comparative analysis of various modelling techniques for emission prediction of diesel engine fueled by diesel fuel with nanoparticle additives§

Erdi Tosun[1*], Tayfun Ozgur[2], Ceyla Ozgur[2], Mustafa Ozcanli[2], Hasan Serin[2], Kadir Aydin[2]

[1]Çukurova University, Department of Mechanical Engineering, Turkey; etosun@cu.edu.tr
[2]Çukurova University, Department of Automotive Engineering, Turkey; tozgur@cu.edu.tr, kdraydin@cu.edu.tr, ozcanli@cu.edu.tr

Abstract

In this study, emissions of compression ignition engine fueled by diesel fuel with nanoparticle additives was modeled by regression analysis, artificial neural network (ANN) and adaptive neuro fuzzy inference system (ANFIS) methods. Cetane number (CN) and engine speed (rpm) were selected as input parameters for estimation of carbon monoxide (CO), oxides of nitrogen (NOx), and carbon dioxide (CO_2) emissions. The results of estimation techniques were compared with each other and they showed that regression analysis was not accurate enough for prediction. On the other hand, ANN and ANFIS modelling techniques gave more accurate results with respect to regression analysis; linear and non-linear. Especially ANFIS models can be suggested as estimation method with minimum error compared to experimental results.

Keywords: Adaptive neuro fuzzy inference system; Artificial neural network; Diesel engine; Regression analysis

1. INTRODUCTION

In recent years, depletion of fossil fuels forces researchers to search new alternative fuels. In literature, there are a lot of studies about fuels which have potential to replace fossil fuels used in internal combustion engines. In this respect, various biofuels and alcohols seem as good option [1]. In addition to scarcity of conventional fuels, efforts on performance en-hancement and emission reduction of engines are the other important issues on which engineers and engine manufacturers are working on it. Especially, the stringent emission legislations enforced manufacturers to develop new technologies [2]. Traditional engine research and development studies are both difficult and costly to meet emission limits imposed by legislations. Therefore, these costly studies are replaced by various cost-effective approaches as artificial neural networks (ANN) and computational fluid dynamics (CFD) [3]. ANNs are nonlinear computer algorithms, which can model the behavior of complex nonlinear processes. Recently, this method has been widely applied to various disciplines as automotive engineering [4]. Yusaf et al. studied the effect of using CPO (crude palm oil) - OD (ordinary diesel) blends as fuel on the performance of CI (compression ignition) engine. In addition, engine power output, fuel consumption, and exhaust-gas emission are evaluated and then predicted using ANN technique [5]. Shanmugam et al. used ANN modeling to predict the performance and exhaust emissions of the diesel engine using hybrid fuel and they revealed that the ANN approach could be confidently used to predict the performance and emissions of the diesel engine accurately [6]. Ghazikhani and Mirzaii predicted soot emission of a waste-gated turbo-charged DI diesel engine using ANN. The results showed the ANN approach can be used to accurately predict soot emis-sion of a turbo-charged diesel engine in different opening ranges of waste-gate (ORWG) [7].

On the other hand, there is another modelling approach called as adaptive neuro fuzzy inference system (ANFIS) which combines the benefits of ANNs and fuzzy logic. ANFIS modelling is very powerful technique with the ability of interpretable if-then rules [8]. Isin and Uzunsoy presented fuzzy logic-based prediction method to reveal the performance and emission characteristics of a single cylinder spark ignition (SI) engine, which uses different fuel mixtures [9]. Ozkan et al. used ANFIS to estimate the effect of methanol mixtures in different proportions on emission and performance of the motor [10]. Al-Hinti et al. used a neuro-fuzzy interface system to study the effect of boost pressure on the efficiency, brake mean effective pressure (BMEP), and the brake specific fuel consumption (BSFC) of a single cylinder diesel engine.

*Corresponding authour
Email: etosun@cu.edu.tr (E.Tosun)
§ This paper was presented at the IMSEC-2016

Results of their study showed that the ANFIS technique can be used adequately to identify the effect of boost pressure on the different engine characteristics.

In this study, experimental studies were taken from the study of Ozgur [12]. He investigated effects of addition of oxygen containing nanoparticle additives to diesel and biodiesel fuels on diesel and biodiesel fuel properties and effects on diesel engine performance and emissions. This study aims to predict exhaust emissions of diesel engine by various approaches as regression analysis, ANN, ANFIS. Finally, performances of models were determined by comparing experimental values and the best estimation technique was stated.

2. MATERIALS AND METHODS

2.1 Experimental Studies

Engine performance tests were performed on a commercial four cylinder, four-stroke, naturally aspirated, water-cooled direct injection compression ignition engine. Engine gives 89 kW maximum power at 3200 rpm and 295 Nm maximum torque at 1800 rpm engine speed. Before the tests, the engine was operated for 15 minutes with diesel fuel to reach the operation temperature. A hydraulic dynamometer was used for determination of torque output. TESTO 350 XL gas analyzer was used to measure exhaust emissions. Emission data was collected by the help of a computer program. Measurement accuracy of the gas analyzer is ±10 ppm for CO, 1% for CO_2 and ±1 ppm for NOx. Measurement capacity of the device is 0-10000 ppm for CO, 0-50% for CO_2 emission and 0-3000 ppm for NOx. The speed sensor used to detect prime mover speed is the magnetic pickup (MPU). When a magnetic material (usually a gear tooth driven by the prime mover) passes through the magnetic field at the end of the magnetic pickup, a voltage is developed. The frequency of this voltage is translated by the speed into a signal which accurately depicts the speed of the prime mover. The Cetane number and indexes were measured by Zeltex ZX440 type device, which works under the close infrared spectrometer (NIR) principal. With the help of this principal the Cetane number measurement experiment became very fast and cheap with only 3% error compared to the time consuming expensive motor tests.

2.2 Regression Analysis

Regression analysis is commonly used to define quantitative relationships between a response variable and one or more explanatory variables [13]. Regression analysis can be applied to the data in linear and non-linear forms.

Linear relationship between dependent and independent variables can be expressed in form of [14]:

$$Y = \beta_0 + \beta_1 X_1 + \beta_2 X_2 + \cdots + \beta_n X_n \quad (1)$$

where is dependent variable, to are equation parameters for linear relationship and to are independent variables.

Nonlinear regression is a form of regression analysis in which observational data are modeled by a nonlinear combination of the model parameters function. Non-linear relationship between dependent and independent variables can be expressed in form of [14]:

$$Y=a_0\left(X_1^{a_1}\right)\left(X_2^{a_2}\right)\cdots\left(X_n^{a_n}\right) \quad (2)$$

where is dependent variable, to are equation parameters for non-linear relationship and to are independent variables.

2.3 Artificial Neural Network

Artificial neural networks inspired by biological neural networks. They behave like human brain. As the brain, ANNs consist of many small, interconnected units [15]. These units called as neuron. A typical biological neuron was shown in Fig. 1.

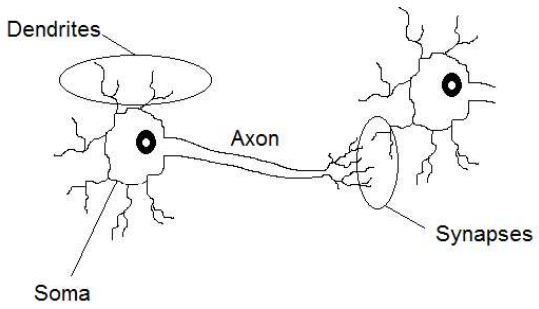

Figure 1: A typical biological neuron.

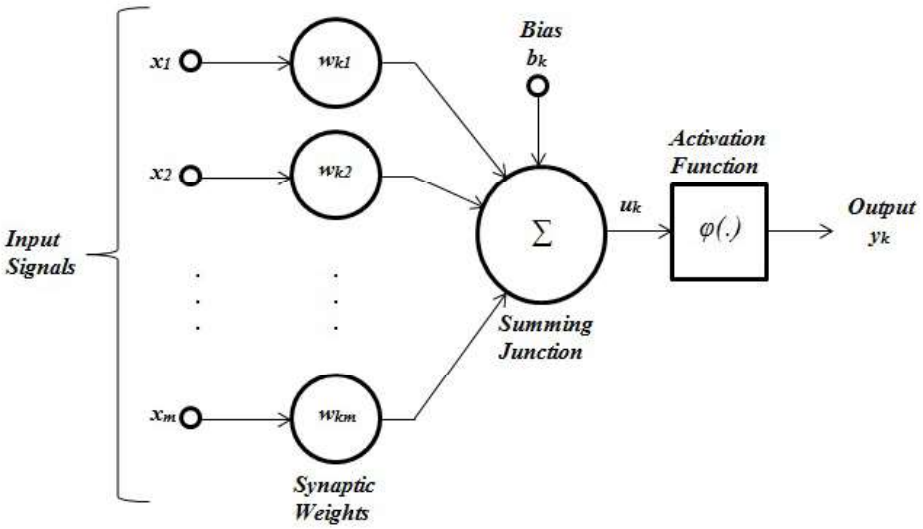

Figure 2: Block diagram of model of ANN neuron [16].

Haykin stated mathematically that, we can describe a neuron k by the following equations [16]:

$$u_k = \sum_{j=1} w_{kj} x_j \tag{3}$$

$$y_k = \varphi\left(u_k + b_k\right) \tag{4}$$

Bias, denoted by bk, has the effect of increasing or lowering the net input of the activation function. x_1, x_2, …, x_m are the inputs; w_{k1}, w_{k2}, …, w_{km} are the weights of the neuron k; u_k is the linear combiner output due to input signals; φ(.) is the activation function; y_k is the output signal of the neuron.

2.4 Adaptive Neuro Fuzzy Inference System

Adaptive Neuro Fuzzy Inference System (ANFIS) is combination system of neural networks and fuzzy logic and it has been applied to various application areas and gives more accurate results with respect to conventional techniques [17]. In fuzzy logic, nonlinearity and complexity of modelling can be handled by rules, membership functions and inference processes [9]. ANFIS can construct set-of if-then rules with suitable membership functions to constitute input-output pairs [18].

Jang presented the basics of fuzzy inference system that uses neural network learning algorithm [18]. Fig. 3 shows the main architecture of ANFIS. In this figure, fuzzy inference system with two inputs (x, y) and one output (z) was considered. According to Takagi and Sugeno type inference system, following two fuzzy if-then rules has been supposed:

Rule 1: If x is A_1 and y is B_1 then $f1=p_1x+q_1y+r_1$

Rule 2: If x is A_2 and y is B_2 then $f2=p_2x+q_2y+r_2$

x and y are the input nodes, A and B are linguistic variables (small, large etc.) associated with this node function.

More detail about the layers of the structure can be found in the study of Jang [18].

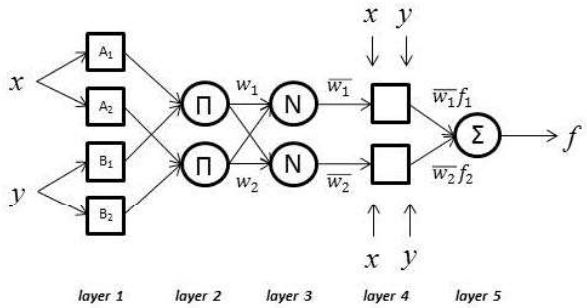

Figure 3: Architecture of ANFIS [18]

2.5 Details of Models

2.5.1 Regression Models

SPSS software was used to perform regression analysis. It is well-known statistical and data management program. Cetane number (CN) and engine speed (rpm) was selected as predictor (independent) variables. Linear and non-linear form of regression analysis was evaluated separately. The results of the analysis were given in Table 1.

Table 1 The results of regression analysis

Y	Linear Regression			Non-linear Regression		
CO	109.993	-1.228	0.099	2.818	-0.089	0.636
NOx	1288.84	5.489	-0.247	11614.49	0.325	-0.484
CO2	8.726	0.03	-0.002	66.37	0.255	-0.428

2.5.2 ANN Models

Data set was generated by using the experimental results of previous study of Ozgur [12]. Then, the total data set was divided into two parts, training and testing data. Training part of data was for about 85% of total data. Remaining randomly selected 15% of total data was used to measure the estimation performance of model as testing.

Matlab software was used to perform ANN modelling. The ANN architecture was consisted of input, hidden and output layer as shown in Fig. 4.

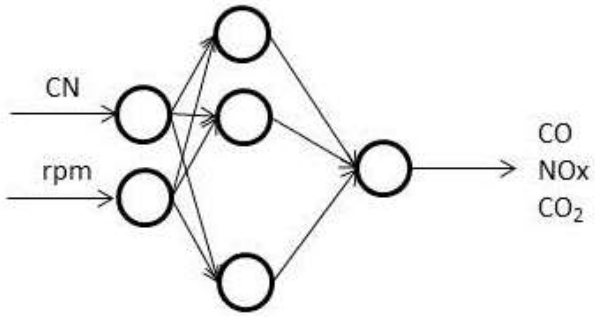

Figure 4: Architecture of ANN

Learning algorithm of the present study is Levenberg–Marquardt (LM) algorithm. Logistic sigmoid transfer function (logsig) and linear transfer function (purelin) were used in the hidden layers and output layer of the network as an activation function, respectively. There was an input layer, hidden layer and output layer. Table 2 shows the architecture of ANN models for each estimated parameters.

Table 2 Architecture of ANN models

Estimation	Learning Algorithm	ANN Structure	Hidden Layer Transfer Function	Output Layer Transfer Function
CO	LM	2-30-1	logsig	purelin
NOx	LM	2-21-1	logsig	purelin
CO2	LM	2-19-1	logsig	purelin

Since there was not a certain number of hidden layer neuron, number of hidden layer was determined by trial and error method. Suitable numbers of hidden layer neuron was supplied in above Table 2.

2.5.3 ANFIS Models

Matlab software was used to perform ANFIS modelling. As ANN modelling, the total data set was divided into two parts, training and testing data. Similar to determining the number of hidden layer neuron, there is no basic rule to define the number and type of membership functions for input parameters. It is an iterative process [17]. Table 3 shows the architecture of ANN models for each estimated parameters.

Table 3 Architecture of ANFIS models

Estimation	Input		Output
	MF number	MF type	MF type
CO	4 4	trimf	linear
NOx	4 4	trimf	linear
CO2	5 5	trimf	constant

3. RESULTS AND DISCUSSIONS

In the following figures, testing periods of the each estimation method for CO, NOx and CO_2 were supplied.

In CO prediction, the worst estimation technique was linear regression with 9.41% error value with respect to experimental data. On the other hand, ANFIS is the best estimation technique with 4.89% error.

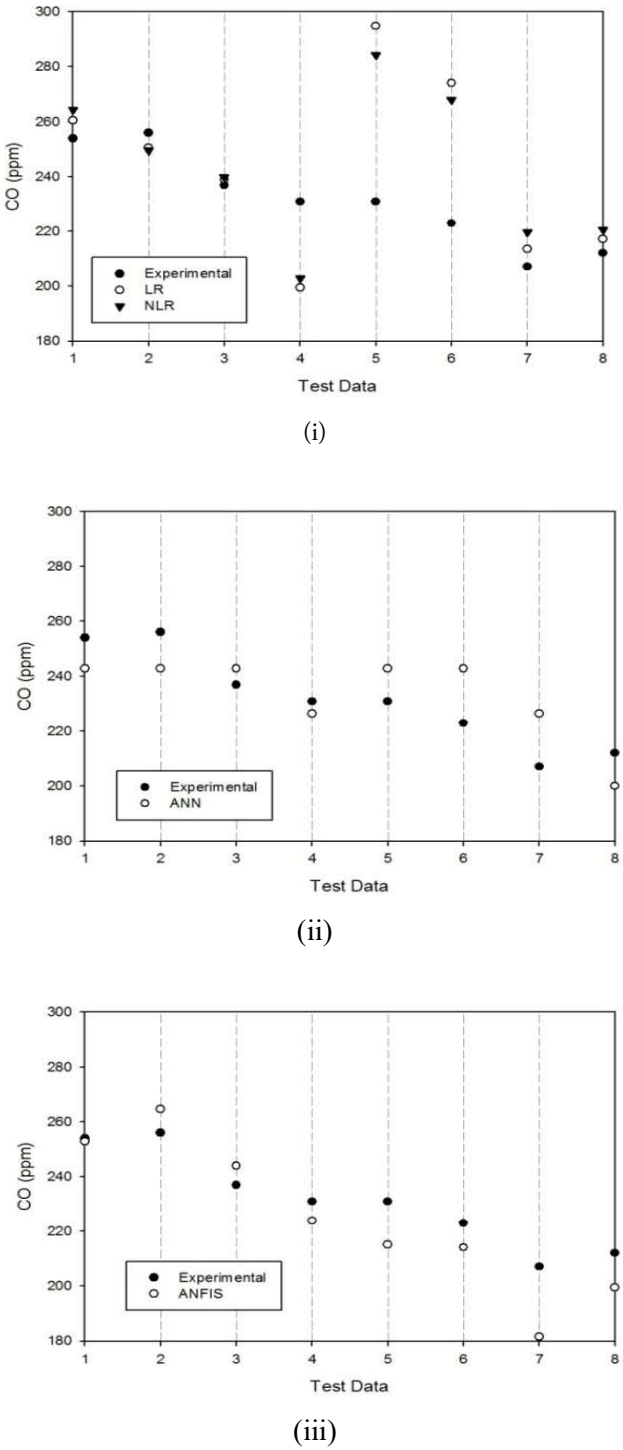

Figure 5: Testing Results of (i) regression analysis (ii) ANN (iii) ANFIS for CO

In testing period of NOx prediction, linear regression is worst and ANFIS is best prediction method with 5.65% and 2.72% error, respectively.

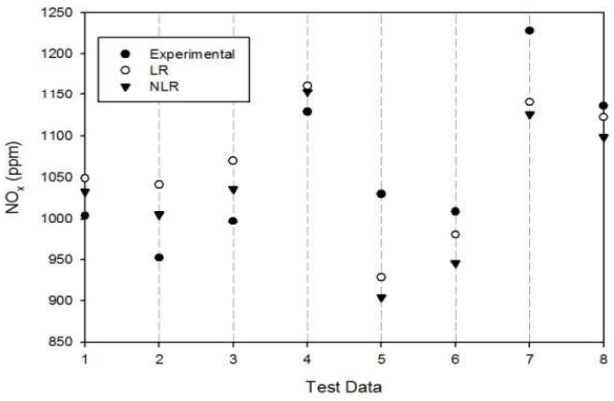

(iv)

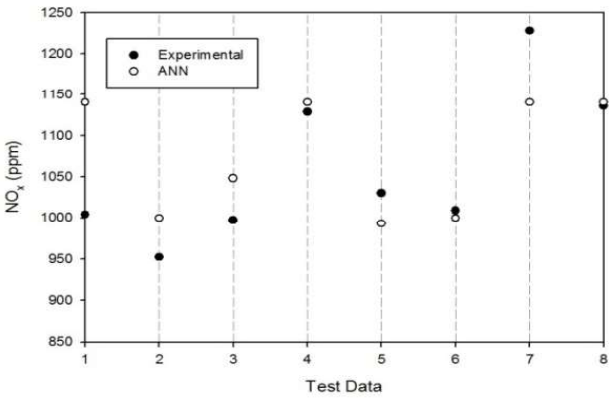

(v)

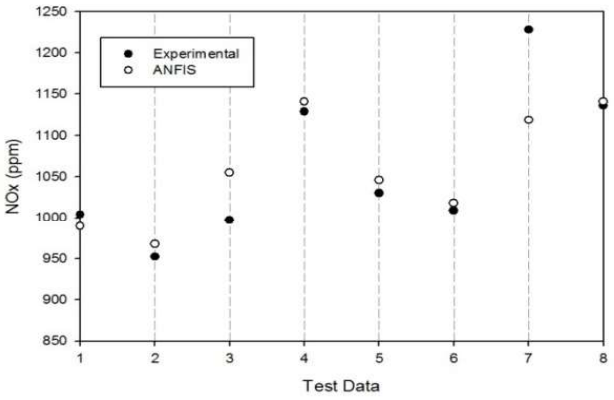

(vi)

Figure 6: Testing Results of (iv) regression analysis (v) ANN (vi) ANFIS for NOx

In CO_2 prediction, the worst estimation technique was linear regression with 17.6% error value with respect to experimental data. ANFIS is the best estimation technique with 3.1% error.

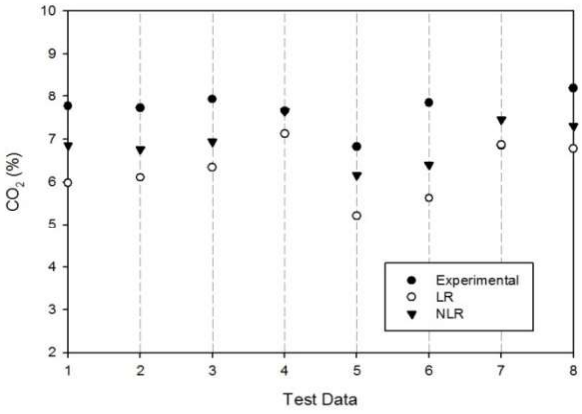

(vii)

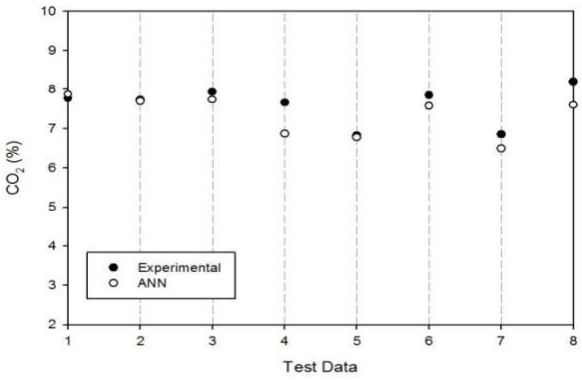

(viii)

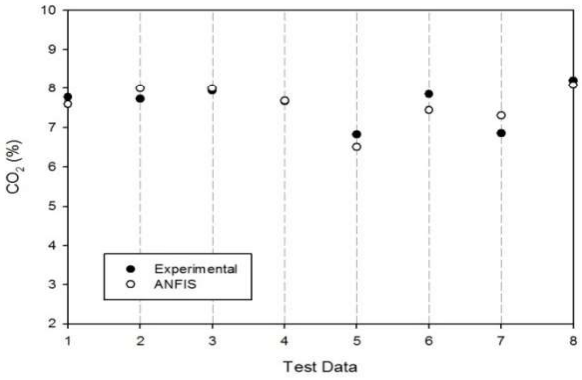

(ix)

Figure 7: Testing Results of (vii) regression analysis (viii) ANN (ix) ANFIS for CO_2

Figs. 5, 6 and 7 showed the testing period of various modelling approaches for CO, NOx and CO_2 emissions, respectively. All predictions were compared with experimental values. Table 4 reveals the performance of both training and testing period of each model for each estimation parameter. Mean absolute percentage error (MAPE) was used as performance parameter.

Table 4 MAPE values of models for both training and testing

		MAPE (%)	
		Training	Testing
CO	LR	16.19	9.41
	NLR	14.94	9.16
	ANN	14.81	5.39
	ANFIS	1.5	4.89
NOx	LR	8.87	5.65
	NLR	9.84	5.59
	ANN	9.58	4.6
	ANFIS	1.82	2.72
CO_2	LR	16.61	17.6
	NLR	13.33	10.63
	ANN	7.86	3.91
	ANFIS	4.12	3.1

4. CONCLUSIONS

The purpose of this paper is to estimate emission of diesel engine by using cetane number of fuel and engine speed. In this respect, three different methods called as regression analysis, ANN and ANFIS were developed for prediction. Data were divided into two parts, training and testing. In training section model details were identified by using experimental data. In testing section, the accuracy and performance of the models were tested. For both emissions, LR and NLR gave worst results. It can clearly be seen from the Table 4. ANN models were more acceptable than regression results. Furthermore, ANFIS approach provided better performance then both regression analysis and ANN.

REFERENCES

[1] Tosun, E., Yilmaz, A.C., Ozcanli, M., and Aydin, K. (2014). Determination of effects of various alcohol additions into peanut methyl ester on performance and emission characteristics of a compression ignition engine. Fuel, vol. 126, pp. 38-43. 10.1016/j.fuel.2014.02.037

[2] Hussain, J., Palaniradja, K., Alagumurthi, N., and Manimaran, R. (2012). Effect of exhaust gas recirculation (EGR) on performance and emission characteristics of a three cylinder direct injection compression ignition engine. Alexandria Engineering Journal, vol. 51, no. 4, pp. 241-247. 10.1016/j.aej.2012.09.004

[3] Ismail, H.M., Ng, H.K., Queck, C.W., and Gan, S. (2012). Artificial neural networks modelling of engine-out responses for a light-duty diesel engine fuelled with biodiesel blends. Applied Energy, vol. 92, pp. 769-777. 10.1016/j.apenergy.2011.08.027

[4] Jahirul, M., Saidur, R., Masjuki, H., Kalam, M., and Rashid, M. (2009). Application of artificial neural networks (ANN) for prediction the performance of a dual fuel internal combustion engine. HKIE Transactions, vol. 16, no. 1, pp. 14-20.

[5] Yusaf, T., Yousif, B., and Elawad, M. (2011). Crude palm oil fuel for diesel-engines: experimental and ANN simulation approaches. Energy, vol. 36, no. 8, pp. 4871-4878. 10.1016/j.energy.2011.05.032

[6] Shanmugam, P., Sivakumar, V., Murugesan, A., and Ilangkumaran, M. (2011). Performance and exhaust emissions of a diesel engine using hybrid fuel with an artificial neural network. Energy Sources, Part A: Recovery, Utilization, and Environmental Effects, vol. 33, no. 15, pp. 1440-1450.

[7] Ghazikhani, M. and Mirzaii, I. (2011). Soot emission prediction of a waste-gated turbo-charged DI diesel engine using artificial neural network. Neural Computing and Applications, vol. 20, no. 2, pp. 303-308. 10.1007/s00521-010-0500-7

[8] Hosoz, M., Ertunc, H.M., Karabektas, M., and Ergen, G. (2013). ANFIS modelling of the performance and emissions of a diesel engine using diesel fuel and biodiesel blends. Applied Thermal Engineering, vol. 60, no. 1, pp. 24-32. 10.1016/j.applthermaleng.2013.06.040

[9] Isin, O. and Uzunsoy, E.U. (2013). Predicting the Exhaust Emissions of a Spark Ignition Engine Using Adaptive Neuro-Fuzzy Inference System. Arabian Journal for Science and Engineering, vol. 38, no. 12, pp. 3485-3493. 10.1007/s13369-013-0637-7

[10] Özkan, İ.A., Ciniviz, M., and Candan, F. (2015). Estimating Engine Performance and Emission Values Using ANFIS/ANFIS Kullanılarak Motor Performans ve Emisyon Değerleri Tahmini. International Journal of Automotive Engineering and Technologies, vol. 4, no. 1, pp. 63-67.

[11] Al-Hinti, I., Samhouri, K., Al-Ghandoor, A., and Sakhrieh, A. (2009). The effect of boost pressure on the performance characteristics of a diesel engine: A neuro-fuzzy approach. Applied Energy, vol. 86, no. 1, pp. 113-121. 10.1016/j.apenergy.2008.04.015

[12] Özgür, T. (2011) Investigation of nanoparticle additives to the biodiesel and diesel fuels for improvement of the performance and exhaust emissions in a compression ignition engine, M.Sc. Thesis, Mechanical Engineering, Cukurova University.

[13] Tabari, H., Kisi, O., Ezani, A., and Talaee, P.H. (2012). SVM, ANFIS, regression and climate based models for reference evapotranspiration modeling using limited climatic data in a semi-arid highland environment. Journal of Hydrology, vol. 444, pp. 78-89. 10.1016/j.jhydrol.2012.04.007

[14] Bilgili, M., Sahin, B., Yasar, A., and Simsek, E. (2012). Electric energy demands of Turkey in residential and industrial sectors. Renewable and Sustainable Energy Reviews, vol. 16, no. 1, pp. 404-414. 10.1016/j.rser.2011.08.005

[15] Krauss, G., Kindangen, J.I., and Depecker, P. (1997). Using artificial neural networks to predict interior velocity coefficients. Building and Environment, vol. 32, no. 4, pp. 295-303. 10.1016/S0360-1323(96)00059-5

[16] Haykin, S.S., (2001) Neural networks: a comprehensive foundation. Tsinghua University Press.

[17] Karimi, S., Kisi, O., Shiri, J., and Makarynskyy, O. (2013). Neuro-fuzzy and neural network techniques for forecasting sea level in Darwin Harbor, Australia. Computers & Geosciences, vol. 52, pp. 50-59. 10.1016/j.cageo.2012.09.015

[18] Jang, J.S.R. (1993). Anfis - Adaptive-Network-Based Fuzzy Inference System. IEEE Transactions on Systems Man and Cybernetics, vol. 23, no. 3, pp. 665-685. Doi 10.1109/21.256541

European Mechanical Science 2017, Vol. 1(1): 24-30
Original Paper

The lateral inhibition as conditional entropy enhancer§

Sefa Yıldırım[1*], Zulfiye Arikan[2], Serhan Ozdemir[2]

[1]Çukurova University, Mechanical Engineering Department, Turkey
[2]Izmir Institute of Technology, Turkey

Abstract

Three kinds of redundant sensing have appeared to be utilized by the majority of living beings. Of these, the most remarkable feature of distributed sensor networks is the lateral inhibition (LI), where sensors output in proportion to its own excitation and each sensor negatively influences its nearest neighbors. This brings about local effects such as contrast enhancement, two-point discrimination, and funneling.
In information theory, entropy is a measure of the uncertainty related to a random variable. Shannon entropy, quantifies the anticipated value of the information included in a message, usually in units such as bits.
The purpose of this study is to analyze lateral inhibition mechanism in the light of the Shannon entropy. This biological mechanism can be adapted to any artificial system such as sensory networks. With the aim of adapting this biological mechanism to the sensory networks it is desired to create an information filter with the benefits of information filter feature of lateral inhibition mechanism. The information has to be quantified in order to filter. In this point, the Shannon entropy concept is intended to be used.

Keywords: Lateral inhibition, mutual information, Shannon entropy, sensory network.

1. INTRODUCTION

The system, which is defined as a distributed sensory network (DSN) and consists of a set of geographically scattered sensors, is utilized in order to collect data from its environment. DSN can be adapted to many advanced systems such as robotics, automation, aerospace etc. Although this system is very practical in applications, it has some drawbacks. In DSN, the redundancy is the most important problem to be solved since it is the main cause of long processing time and extreme processing energy. In highly redundant sensing, redundancy means that transferred information via different sensors or the same sensor at different times overlaps [1]. At that point, Lateral Inhibition (LI) with its simplicity and ubiquity is one way to overcome redundancy with the benefits of its low pass filter feature.

Ernst Mach was the first person having attempted to describe the lateral inhibition based on his experiments. Hartline et al. introduced lateral inhibition by analyzing the facetted compound eye of Horseshoe crab (Limulus)[2]. Barlow was a student of Hartline continued his study on Horseshoe crab and investigated influence of lateral inhibition on its behavior[3]. Georg von Békésy found a large spectrum of inhibitory incidents in sensory systems, and explained them in the sense of sharpening. He explored methodical effects of lateral inhibition in all aspects of human sensing, especially on hearing[4]. Brooks discussed that lateral inhibition may be adapted to robotics[5].

Information could be defined as a representation of knowledge. Information being transferred via sensor signals contains also noise and unnecessary data. For an efficient transmission, it requires to be filtered. An information filter could be used to filter the undesired information. To filter the information, first of all, it needs to be quantified. Claude E. Shannon introduced entropy, an evaluation of uncertainty concerned with random variables, is used to measure the anticipated value of the information. Entropy can be used in order to quantify information[6].

Harry Nyquist explained that communication channels had maximum data transmission rates, and formulated a method to compute those rates in finite bandwidth noiseless channels[7]. Nyquist's colleague Ralph V.L. Hartley used the information word as a measureable amount and established the first mathematical foundations for the information theory[8]. Claude E. Shannon, considered father of information theory, described entropy as the fundamental measure of information[6].

The present paper concerns with the formulation of lateral inhibition mechanism as an information filter. By applying lateral inhibition mechanism to sensory network, it is focused on filtering the unnecessary information thanks to the

*Corresponding authour
Email: syildirim@cu.edu.tr (S. Yıldırım)
§ This paper was presented at the IMSEC-2016

low pass filter feature of lateral inhibition in the light of Shannon entropy concept. The main purpose is to get efficient noiseless information by using inferior quality cheap sensors through lateral inhibition, instead of expensive and quality sensors.

2. LATERAL INHIBITION

Lateral inhibition is the most important feature of the biological distributed sensory network. In this mechanism each sensor effects its nearest neighbors negatively resulting in contrast enhancement, two-point discrimination and funneling. Fig. 1 shows schematic of lateral inhibition mechanism[5].

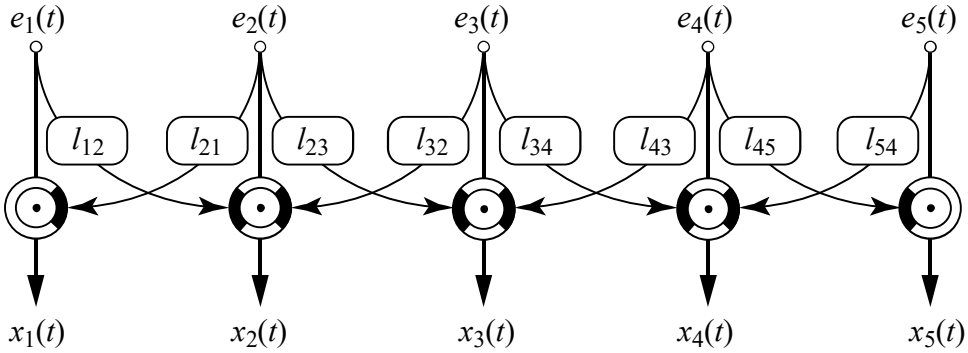

Figure 1: Lateral inhibition schematic

The strengths of the connections, as shown above, are generally put in order as excitant among adjacent receptors and inhibitory among further receptors. To state the matter differently, if one sensor signal is considered, contrary to what the excitatory connections try to do, inhibitory connections try to decrease its signal. As a result, all sensors in the network receive a mixture of inhibitory and excitatory signals from their neighbors. Hence distinction between signals of the sensors which have the strongest output and signals of the sensors which have the weaker output become higher due to this competitive work[9].

In the Fig. 1, the impulse of the sensor before the lateral inhibition is illustrated as *e*, the result of competitive work is demonstrated by *I* which is called effect of lateral inhibition. The impulse of the sensor after the lateral inhibition is illustrated by *x* which is weaker than *e*. Due to the inhibitory and excitatory coefficients and number of neighbors' *x* can vary all the network.

2.1 Mathematical Formulation of Lateral Inhibition

The mathematical formulation of LI was obtained from experiments based on Hartline study on the visual system of Horseshoe Crab[2]. The results are summarized considering two neighbor sensors *A* and *B* in the following mathematical formulas:

$$x_A = e_A - \beta_{AB}(x_B - x_B{}^0)$$
$$x_B = e_B - \beta_{BA}(x_A - x_A{}^0) \qquad \text{(1 a-b)}$$

where x_A and x_B are after inhibition mechanism impulses, e_A and e_B are individual impulses and $x_A{}^0$ and $x_B{}^0$ are threshold frequencies of *A* and *B* respectively. Also β_{AB} is inhibition coefficient of *B* on *A* and β_{BA} is inhibition coefficient of *A* on *B*. These results can be extended to cases where one sensor has two or more neighboring sensors. For example sensors mentioned before(*A* and *B*) have another neighbor *C*, three equations should be required to determine the responses of each sensor. Each equation must contain two inhibition terms as:

$$x_A = e_A - [\beta_{AB}(x_B - x_{AB}{}^0) + \beta_{AC}(x_C - x_{AC}{}^0)]$$
$$x_B = e_B - [\beta_{BC}(x_C - x_{BC}{}^0) + \beta_{BA}(x_A - x_{BA}{}^0)] \qquad \text{(2 a-c)}$$
$$x_C = e_C - [\beta_{CA}(x_A - x_{CA}{}^0) + \beta_{CB}(x_B - x_{CB}{}^0)]$$

Here β_{ij} are inhibition coefficients among *A, B* and *C*.When equations are extended to define the effect of lateral inhibition mechanism on n number of sensor and self-excitatory influences are considered, they are transformed into following form;

$$x_p = e_p + \alpha_p e_p - \sum_{j=1}^{n} \beta_{pj} x_j \quad (3)$$

where; α is the self-excitation coefficient of sensors, p=1,2,3,...,n; $j \neq p$ and α>0 and β>0 All threshold frequencies are assumed zero for simplicity [9].

3. ENTROPY (IN INFORMATION THEORY)

Information could be defined as a representation of knowledge. Entropy was introduced as a measure of the uncertainty related to a random variable which quantifies the expected value of the information contained in a message, usually in units such as bits or nats[6]. Shannon entropy concept measures inadequate information and define the uncertainty[10]. Formulation of Shannon entropy, the entropy of a random variable X, is illustrated below;

$$H(X) = -\sum_{x \in X} P(x) log_2 P(x) \quad (4)$$

where $P(x)$ denotes probability of x. If the entropy of the signal is low, it means that probable quantities are abundantly obtained.

4. MUTUAL INFORMATION

Mutual information, is a dimensionless quantity with units of bits, measures the information of one random variable about another random variable. It can be considered as the reduction in uncertainty about one random variable given knowledge of another[11]. This phenomenon can be described with Fig. 2. illustrated below.

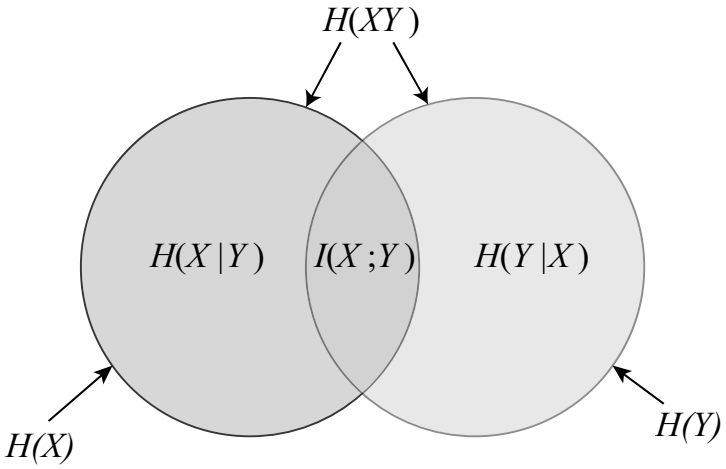

Figure 2: Description of mutual information

In this figure, $I(X;Y)$ depicts the mutual information of X and Y, and can be calculated as below:

$$I(X;Y) = H(X) - H(X|Y) = \sum_{x \in X} \sum_{y \in Y} P(x,y) log \frac{P(x,y)}{P(x)P(y)} \quad (5)$$

where $H(X)$ is uncertainty of X and $H(X|Y)$ is uncertainty of X given knowledge of Y.

If one system has a LI mechanism, mutual information certainly exists in this system and only sensors which have mutual information are active. Note that amount of mutual information depends on position of the sensor.

5. LATERAL INHIBITON AS AN INFORMATION FILTER

The lateral inhibition mechanism filters the mutual information hence there are some important factors to be considered while filtering the information in the sensor networks. First of all, frequency of the obtained information should be taken into consideration as the frequency is related to mutual information. And also characteristic of the desired or undesired information is one of the important factors. For the reliability, distance of the sensor to the source is important and mutual information might be desired to be high.

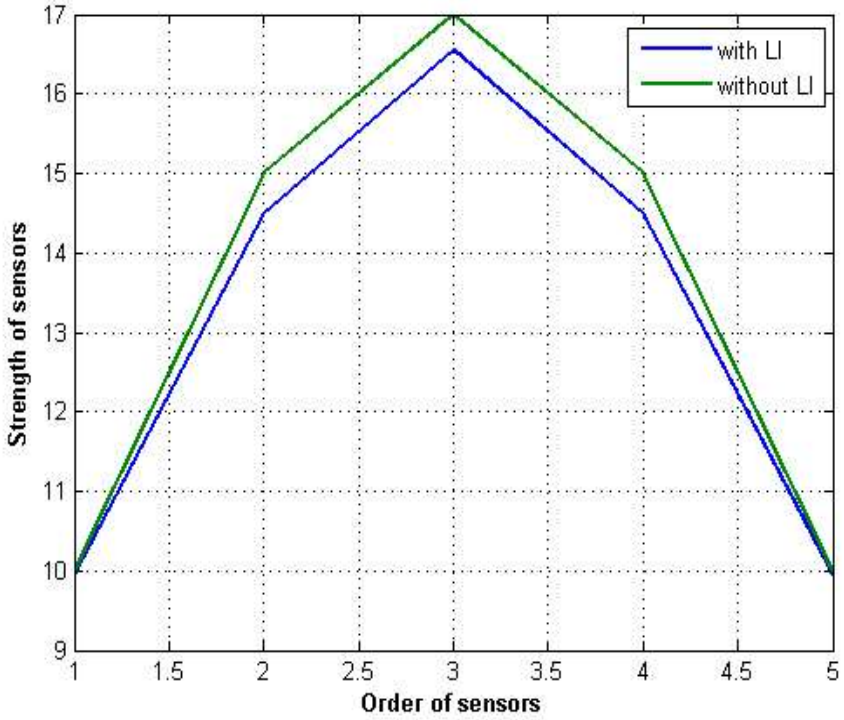

Figure 2: Simulation of the lateral inhibition effect in the sensory network (with 4 neighbors)

In Fig.2 green line represents the sensor signals before the LI and blue line represents the sensor signals after applied LI. As shown above, the lateral inhibition filters the amount of information and increases the contrast. The lateral inhibition is considered to be filtering the mutual information.

5. COMPUTER SIMULATIONS

To simulate effect of the LI on the sensory network, it is considered that there is a group of a scattered photodiodes which is schematically illustrated below and there is a one light source above the central photodiode.

Table 1. Schematic illustration of the simulated sensory network

S	S	S	S	S
S	S	S	S	S
S	S	**S**	S	S
S	S	S	S	S
S	S	S	S	S

In the sensory network it is assumed that all photodiodes have 8 neighbors except located on the borders. The response of the sensors is defined logically as the photodiode which is on the center of the group has maximum strength. The defined sensor strengths without LI are seen from the Table 2 below.

Table 2. Schematic illustration of the defined sensor strengths without LI

7	8	10	8	7
8	14	15	14	8
10	15	17	15	10
8	14	15	14	8
7	8	10	8	7

In this simulation, inhibition coefficient (β) was chosen as 0.05 and the excitation coefficient (α) was chosen as 0.15. The results after applied the LI on the system can be seen in Table 3. After the implementation, the strength of the sensors with and without the LI was compared in Figure 3.

Table 3. Schematic illustration of the sensor strengths after LI

6.5500	6.5000	8.5500	6.5000	6.5500
6.5000	11.6000	12.2000	11.6000	6.5000
8.5500	12.2000	13.7500	12.2000	8.5500
6.5000	11.6000	12.2000	11.6000	6.5000
6.5500	6.5000	8.5500	6.5000	6.5500

With the increase of the number of neighbors, maximum amplitude increases as well. This results in contrast enhancement hence discrimination of a desired object can be easier.

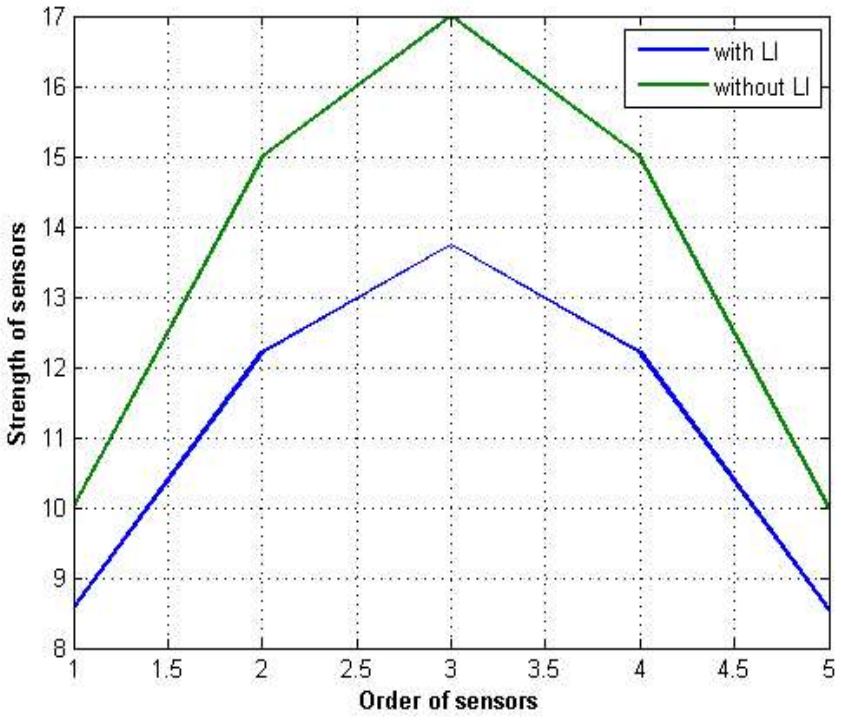

Figure 3: Effect of the lateral inhibition (with 8 neighbors and examined only central sensors)

If it is assumed that two sensors do not work and one of the broken sensor is neighbor of the examined sensors, simulation results can be seen in Table 5 and Figure 4.

Table 4. Strength of the sensor group (two sensors broken)

7	0	10	8	7
8	14	15	14	8
10	15	17	15	10
8	14	15	0	8
7	8	10	8	7

Table 5. Simulation results of a sensor strengths (two sensors broken, shown bold)

6.9500	**-2.7000**	8.9500	6.5000	6.5500
6.9000	12.0000	12.6000	11.6000	6.5000
8.5500	12.2000	14.4500	12.9000	9.2500
6.5000	11.6000	12.9000	**-4.5000**	7.2000
6.5500	6.5000	9.2500	7.2000	7.2500

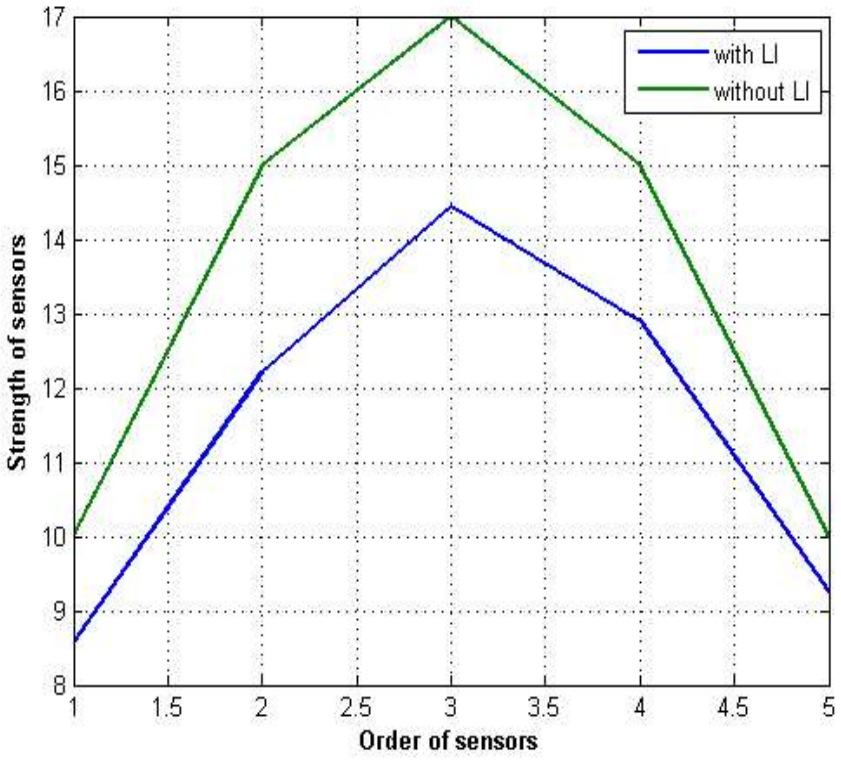

Figure 4: Effect of the lateral inhibition (two sensors broken)

From the Fig. 4, it is seen that there is a decrease from the contrast on the right side of the network therefore it does not prevent all the system to work. Also there is no decrease from the maximum contrast.

It is assumed that this sensory network considered as a group of thermal receptors. Even though a problem occurs on one of the sensors of the group, it still operates well. Also it should take into consideration that constant maximum contrast is crucial part of this advantage.

6. CONCLUSIONS

Lateral inhibition provides a series of advantages to filter undesired information, as well as emphasizing the desired one. Maximum signal intensity decreases after being processed with LI and detected signal sharpens. LI mechanism reduces the number of active sensors and it causes a reduction of the system cost. After LI is applied signal processing speed increases for the same processor and in the case of information storage, memory requirement is reduced. It may even reduce the costs and increase the reliability.

LI has also some disadvantages in practice. LI mechanism is applicable to in multi-sensor networks. This points to the use of a multitude of sensors. Cost of initial investment and overhaul are expected to be high. LI further increases weight and volume of the system.

But the system possesses fault-tolerant structure, in that even one or more sensors break down in the sensory network the system can continue its normal operation without major trouble. This is because mutual information is shared by every individual sensor in the network.

REFERENCES

[1] Coskun, A., Sevil, H.E., and Ozdemir, S. (2011). Cost effective localization in distributed sensory networks. Engineering Applications of Artificial Intelligence, vol. 24, no. 2, pp. 232-237. 10.1016/j.engappai.2010.10.006

[2] Hartline, H.K., Wagner, H.G., and Ratliff, F. (1956). Inhibition in the eye of Limulus. The Journal of general physiology, vol. 39, no. 5, pp. 651-673.

[3] Barlow, R.B. (1969). Inhibitory fields in the Limulus lateral eye. The Journal of general physiology, vol. 54, no. 3, pp. 383-396.

[4] Von Békésy, G., (1967) Sensory inhibition (The Herbert Sidney Langfeld memorial lectures,, no. 1965). Princeton, N.J.,: Princeton University Press, pp. x, 265 p.

[5] Brooks, M., "Highly redundant sensing in robotics—analogies from biology: distributed sensing and learning," in Highly Redundant Sensing in Robotic Systems: Springer, 1990, pp. 35-42.

[6] Shannon, C.E. (2001). A mathematical theory of communication. ACM SIGMOBILE Mobile Computing and Communications Review, vol. 5, no. 1, pp. 3-55.

[7] Nyquist, H. (1924). Certain factors affecting telegraph speed. Transactions of the American Institute of Electrical Engineers, vol. 43, pp. 412-422.

[8] Hartley, R.V. (1928). Transmission of information. Bell Labs Technical Journal, vol. 7, no. 3, pp. 535-563.

[9] Coşkun, A. (2006) Contrast enhancement by lateral inhibition in a sensory network, M.Sc., İzmir Institute of Technology.

[10] Haykin, S.S., (2001) Neural networks: a comprehensive foundation. Tsinghua University Press.

[11] Erdogmus, D., Agrawal, R., and Principe, J.C. (2005). A mutual information extension to the matched filter. Signal Processing, vol. 85, no. 5, pp. 927-935. 10.1016/j.sigpro.2004.11.018

European Mechanical Science 2017, Vol. 1(1): 31-38
Original Paper

Pulsating flow and heat transfer in wavy channel with zero degree phase shift§

Harun Zontul[1*], Nazım Kurtulmuş[2], Beşir Şahin[3]

[1,3]Çukurova University, Mechanical Engineering Department, Turkey
[2]Adana Science and Technology University, Turkey

Abstract

In this study, heat transfer enhancement of laminar pulsating flow in wavy channel is investigated numerically. The wavy channel has constant wall temperature and its geometric parameters are fixed. Finite volume method based on SIMPLE technique is used to solve governing equations. Simulations performed for Reynolds numbers in the range of 200≤Re≤800. The effects of pulsation frequency is investigated for Strouhal numbers, (St) of 0.05, 0.15 and 0.25. The differences between flow structures of pulsating and steady flow are discussed. Results indicate that the pulsating flow significantly enhances heat transfer.

Keywords: Convection heat transfer, internal fluid flow, fluid mixing, pulsating flow, wavy channels,

1. INTRODUCTION

Pulsating flow has attracted the attention of many researchers from view point of its effect on heat transfer. There are many numerical and experimental studies that investigate the heat transfer performance of pulsating flow through the different geometries. Since internal forced convection phenomena has great importance in numerous engineering applications, studies about pulsating flow and heat transfer in channels, ducts and tubes came into prominence.

Researches about heat transfer in flat channels and pipes under pulsating flow condition points out that the effect of pulsating flow is limited in these geometries [1-5]. Depending on flow parameters, heat transfer can be enhanced or reduced. Guo and Sung [1] numerically investigated heat transfer in pipe for the Reynolds number value of 500. Their results showed that for small pulsation amplitude values both heat transfer augmentation and reduction was observed depending on a pulsation frequency. But when pulsation amplitude was large, heat transfer was always enhanced. Chattopadhyay et al. [2] conducted numerical investigation for laminar pulsating flow in a tube. They concluded that pulsating flow has no considerable effect on heat transfer for investigated amplitude and frequency values. Another numerical analysis performed by Rahgoshay et al. [3] for investigation of the effect of flow pulsation on heat transfer in the isothermally heated pipe. In this study nanofluid was used as working fluid. They obtained only small amount of increase in heat transfer within the range of chosen parameters. Pulsating turbulent flow in pipe was numerically investigated by Wanh and Zhang [4]. They observed significant heat transfer enhancement with large pulsation amplitude values. They also showed that there is an optimum Womersley number (Wo) value that maximizes the heat transfer enhancement. Mehta and Khandekar [5] experimentally investigated pulsating laminar flow in square mini-channel.

In their study pulsation amplitude (A_p) and the Reynolds number kept constant and change of heat transfer rate with pulsation frequency was observed. It was found that the low frequency values deteriorates heat transfer and higher frequencies cause a slight improvement in heat transfer.

Unlike its limited performance at flat channels and tubes, this type of flow provides notable heat transfer enhancement for cooling of blunt bodies in channels [6-8]. Moon et al. [6] carried out experimental study to show how flow pulsation effects heat transfer from heated blocks in a channel. Imposing flow pulsation causes considerable increase in heat transfer from blocks and it is observed that rate of heat transfer is dependent on the pulsation frequency and inter block spacing. Ji et al. [7] discussed heat transfer from a square cylinder in pulsating flow. This study revealed the emergence of lock-on regime and its effect on heat transfer for pulsating flow. Results showed that when pulsation frequency is doubled the natural frequency, heat transfer enhancement becomes maximum. Kim et al. [8] numerically simulated cooling of electrical components in channel by using pulsating flow. They stated that there is an optimal frequency value and it depends on the cooled geometry.

*Corresponding authour
Email: hzontul@cu.edu.tr (H. Zontul)
§ This paper was presented at the IMSEC-2016

Another efficient use of pulsating flow is seen at heat transfer from corrugated channels. Studies about corrugated channels are important in terms of investigation the efficiency of pulsating flow in heat exchangers. In the experimental study of Jin et al. [9] characteristic of pulsating flow in triangular channel was observed. They showed the mechanisms that cause heat transfer enhancement in this channel. Nandi and Chattopadhyay [10] performed a numerical study for wavy micro channel. They reported that even at the low Reynolds number value, pulsating flow causes noticeable heat transfer augmentation in this channel. Akdağ et al.[11] numerically investigated heat transfer enhancement capability of laminar pulsating flow with use of nanofluid. Their study indicated that high volume fraction of nanofluid and a low frequency of pulsation enhances heat transfer performance. An extensive numerical study about pulsating flow in wavy channel presented by Jafari et al. [12]. They investigated effect of two different nanofluids, pulsation frequency, amplitude and the Reynolds number. They reported that pulsating flow is more effective for pure fluid than nanofluid and flow oscillation gives better performance at higher Reynolds numbers. They also observed that there is a linear relationship between amplitude of pulsation and heat transfer enhancement. Alawadhi and Bourisli [13] studied periodic vortex shedding caused by pulsating flow inside wavy channel. They stated that when the frequency of pulsation is close to vortex shedding frequency, heat transfer is peaked.

Studies above shows that the structure of geometry where pulsating flow passes through is a key parameter for the rate of heat transfer. Complex geometries like grooved surfaces provide better heat transfer performances under pulsating flow conditions. The present study is motivated to investigate heat transfer enhancement potential of pulsating flow in a sinusoidal grooved channel when there is 0° phase shift between sinusoidal walls. In order to achieve this numerical simulations are performed by solving the governing equations using finite volume approach.

2. PROBLEM DESCRIPTION AND NUMERICAL METHOD

2.1 Definition of Problem

Schematic view of the channel geometry used in the present study is given in Figure 1. The channel is consist of adiabatic flat sections and constant temperature wavy section. Temperature of wavy section (T_s) is differentially higher than inlet temperature of fluid (T_i).

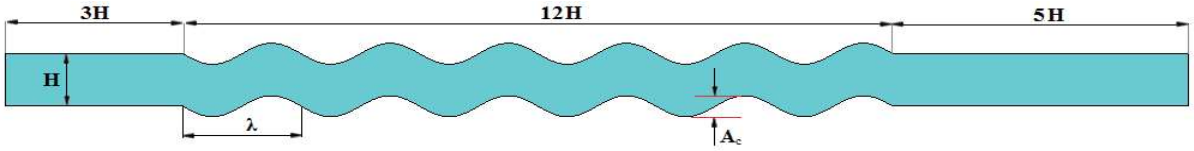

Figure. 1. Schematic view of channel.

Distance between channel walls (H) is considered as 2 cm and profiles of wavy wall defined by:

$$y = A_C \left[\sin\left(2\pi\gamma \frac{x - x_s}{x_e - x_s} \right) \right] \tag{1}$$

Here x_e and x_s represent the starting and ending position of wavy section. Amplitude of wavy wall (Ac) kept constant and its value is 0.2. γ is undulation number.

2.2 Governing Equations

In this study the fluid is taken to be Newtonian, incompressible and its Prandtl number (Pr) is equal to 6.93. The flow is laminar, two dimensional and unsteady. Additionally, gravity effect and thermal radiation are neglected. Under these circumstances non-dimensional form of governing equations becomes,

Continuity equation:

$$\frac{\partial U}{\partial x} + \frac{\partial V}{\partial Y} = 0 \tag{2}$$

Momentum equation:

$$\frac{\partial U}{\partial \tau}+U\frac{\partial U}{\partial X}+V\frac{\partial U}{\partial Y}=-\frac{\partial P}{\partial X}+\frac{1}{Re}\left(\frac{\partial^2 U}{\partial X^2}+\frac{\partial^2 U}{\partial Y^2}\right) \quad (3)$$

$$\frac{\partial V}{\partial \tau}+U\frac{\partial V}{\partial X}+V\frac{\partial V}{\partial Y}=-\frac{\partial P}{\partial Y}+\frac{1}{Re}\left(\frac{\partial^2 V}{\partial X^2}+\frac{\partial^2 V}{\partial Y^2}\right) \quad (4)$$

Energy equation:

$$\frac{\partial \theta}{\partial \tau}+U\frac{\partial \theta}{\partial X}+V\frac{\partial \theta}{\partial Y}=\frac{1}{RePr}\left(\frac{\partial^2 \theta}{\partial X^2}+\frac{\partial^2 \theta}{\partial Y^2}\right) \quad (5)$$

In these equations dimensionless parameters are:

$$(U,V)=\frac{(u,v)}{u_o},\quad (X,Y)=\frac{(x,y)}{H},\quad P=\frac{p}{\rho u_o^2},\quad \theta=\frac{T-T_i}{T_s-T_i},\quad \tau=\frac{tH}{u_o},\quad Re=\frac{\rho u H}{\mu}$$

$$Pr=\frac{C_p\mu}{k}$$

$$\text{Local: } Nu=\left(\frac{-H}{T_s-T_i}\right)\left((\partial T/\partial n)|_{Bottom\,Wall}+(\partial T/\partial n)|_{Top\,Wall}\right) \quad (6)$$

$$\text{Space averaged: } Nu_{\bar{x}}=\frac{1}{(x_e-x_s)}\int_{x_s}^{x_e} Nu\,ds \quad (7)$$

$$\text{Space and period averaged: } Nu_{\bar{\tau}}=\frac{1}{\tau_p}\int_0^{2\pi} Nu_{\bar{x}}\,d\tau \quad (8)$$

Local, space-averaged, space and period timed-averaged Nusselt numbers (Nu) are used for estimation of convection rate from wavy wall. For calculation of the Nusselt number (Nu) instead of bulk temperature, inlet temperature is chosen as a reference parameter [14].

2.3 Boundary Conditions

Fully developed Poiseuille flow with added sinusoidal pulsation term is applied at the channel inlet. Inflow temperature is uniform and steady. Non-dimensional form of inlet velocity profile is presented as:

$$U(Y,\tau)=\frac{3}{2}u_0\left(1-(Y-1)^2\right)\left[1+A_p\sin(2\pi St\tau)\right],\quad V=0,\quad \theta=0 \quad (9)$$

In equation (9) A_p is non-dimensional amplitude, St is the Strouhal number which represents non-dimensional frequency and it is defined as St =fH/uo. The no-slip boundary condition available for channel walls U = V = 0. Straight sections of walls are adiabatic, wavy walls has constant temperature. At the exit of the channel, temperature and velocity gradients are equal to zero , , .

2.4 Numerical Procedure and Code Validation

Finite volume method is employed for discretization of governing equations. Discretization is second order accurate and SIMPLE algorithm used for velocity-pressure coupling. Time step size is set as 0.001 second. For grid independency, grid densities of 60x180, 72x198, 84x252 and 96x288 are tested. Results showed that variation of space averaged Nusselt number () is around 3% between 84x252 and 96x288. Therefore 84x252 grid used in wavy channel. The convergence criterion for continuity, momentum and energy equations is determined as 10^{-5}. The numerical procedure is validated by applying it for the problem defined in the study of Wang and Chen [15]. Agreement between results is presented in Fig. 2.

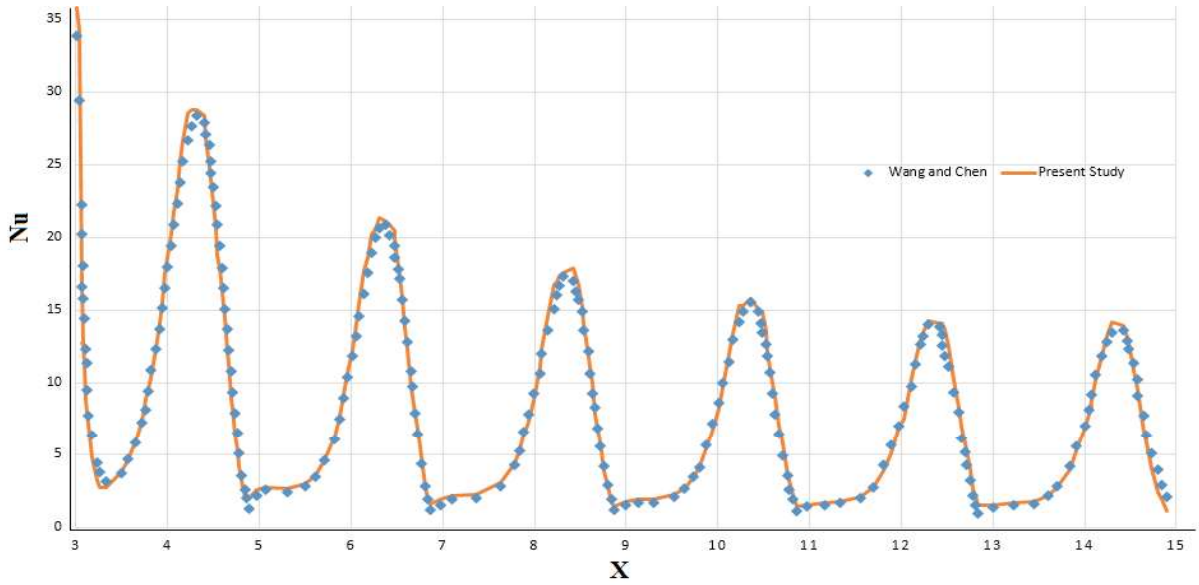

Figure 2. Distribution of Nusselt number (Nu) along bottom wavy wall for Re = 500 and A_c = 0.2.

3. RESULTS AND DISCUSSIONS

Figure 4 shows velocity vectors for steady flow and four different phase angle of pulsating flows. Dimensionless form of inlet mean velocity that corresponds these phase angles can be observed in Figure 5. From the velocity vectors it can be seen that there are vortices trapped inside of grooves. For steady flow, interaction between these vortices and main stream is poor, in other words, mixing between fluid inside grooves and fluid in core region is not effective. In this case high temperature fluid trapped inside grooves.

As it is shown in Figures 4b,c,d and e, flow structures in pulsating flow are quite different from a steady case. At the beginning of the pulsation period (ωt=0), the flow inside grooves is not dominated by a vorticity concentration. There is fluid transfer between the region of grooves and main stream. Afterwards, a complete vortices are developed and rotational speeds raise depending on the flow pulsation period shown in Figures 4c and d. Finally, vorticity concentrations reach their maximum size when phase angle becomes 3π/2, at this state velocity magnitude of flow inside groove is higher as compared to steady flow. As it can be seen in Figure 4e these vortices intensely disturb the main stream. Then they dissipate and flow returns their initial state given in Figure 4a. This situation successively repeats and provides better fluid mixing also prevents trapping of hot fluid inside of grooves.

Temperature distribution in wavy channel for pulsating and steady flow is given in Figure 6. From the figure it can be clearly seen that there is a considerable temperature differences between grooves and area close to central axis for the steady flow. But in pulsating flow hot fluid inside grooves diffuses to the cold region. Consequently, the temperature gradient between channel walls and fluid is increased and heat transfer is enhanced.

Variation of inlet dimensionless velocity (U) with respect to the time causes that the space averaged Nusselt number () varies periodically. For different Strouhal numbers (St), the variation of space averaged Nusselt number for wavy walls is demonstrated in Figure 7. As it is seen in the figure there is a strong relationship between pulsation dimensionless velocity (U) profile and the Nusselt number (). Just like a pulsation of inlet flow, the Nusselt number () reduces at deceleration phase and it increases at acceleration phase. It is obviously seen in figure 7 when Strouhal numbers (St) are equal to 0.15 and 0.25 even the smallest value of the Nusselt number () is higher than the steady case. But for the Strouhal number (St) the value of 0.05, the Nusselt number () becomes lower than the steady case when the inlet velocity decreases; even so, the space and time-averaged Nusselt number () is still higher than the steady case.

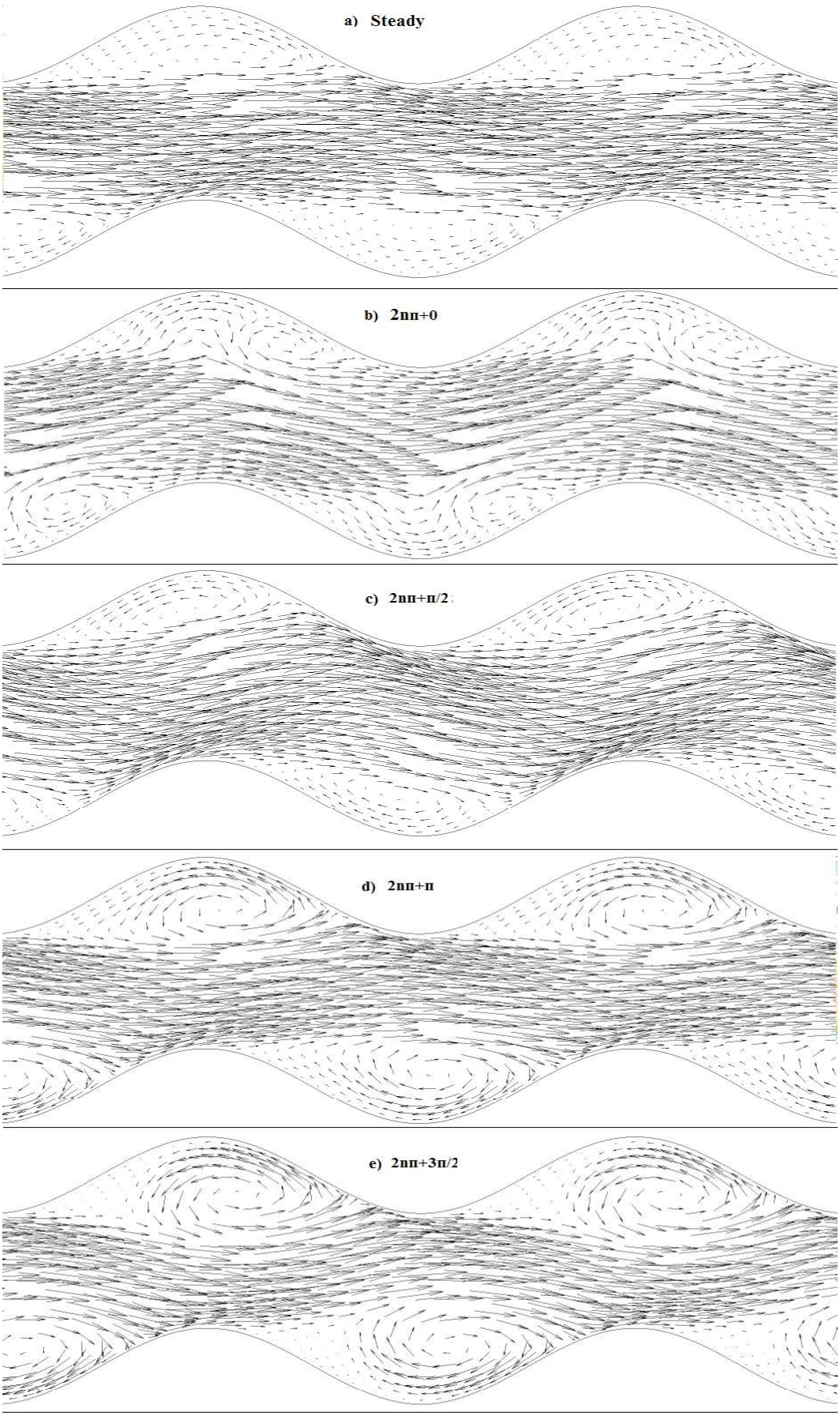

Figure 4**.** Velocity vectors (V) for steady and pulsating flow at Re = 400 and St = 0.25.

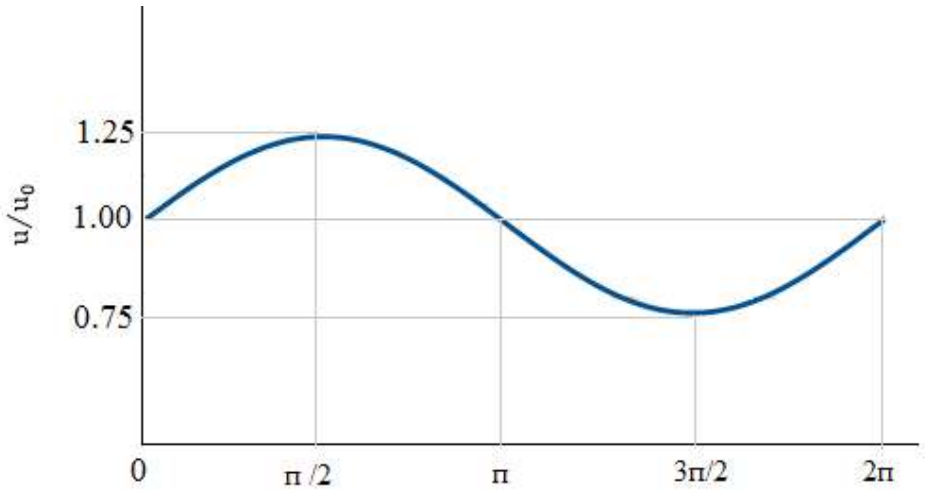

Figure 5 Variation of dimensionless inlet velocity (u/u_0) over a period of cycle

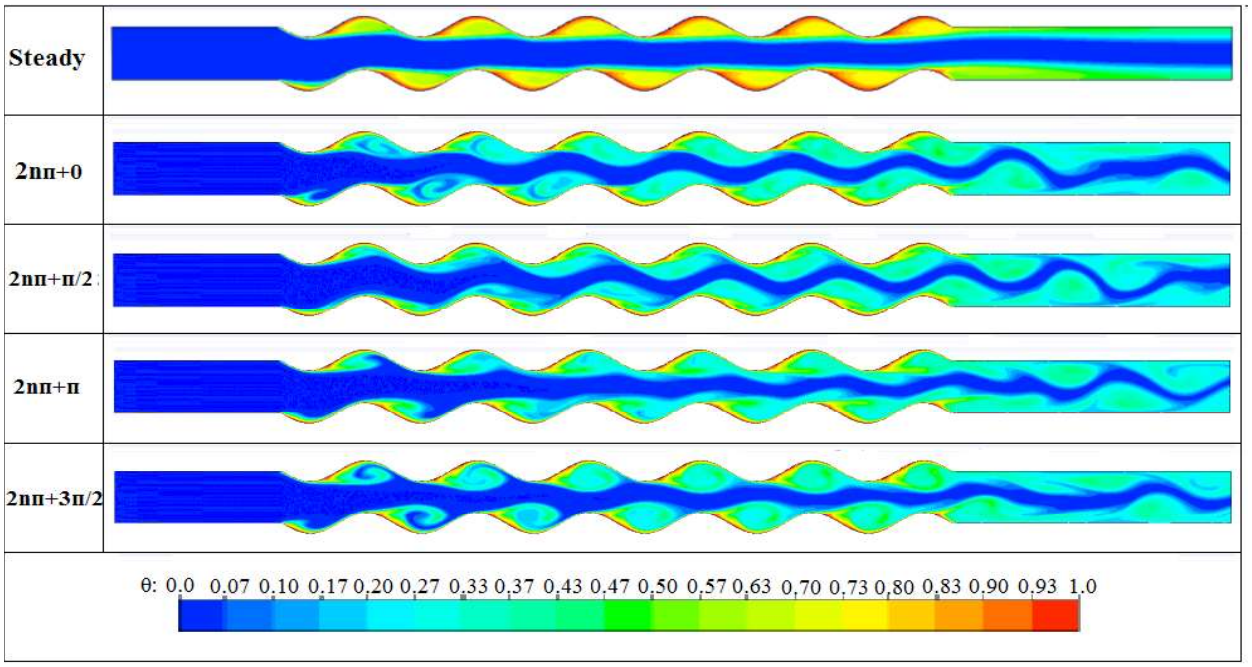

Figure 6 Temperature distribution inside channel for steady and pulsating flow at Re = 400, St = 0.25

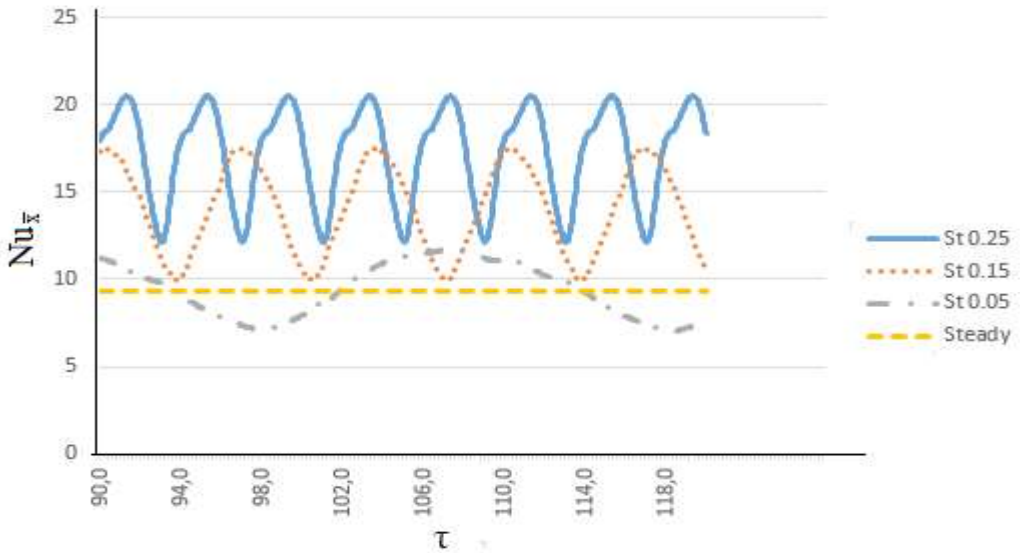

Figure. 7. Variation of the Nusselt number () with time at different Strouhal numbers (St) and Re = 400

In order to investigate heat transfer performance of pulsating flow, the time averaged Nusselt number values are obtained and presented in Figures 8 and 9. Time-averaged Nusselt numbers are calculated when the flow regime reaches the periodic state. Heat transfer enhancement ratio of pulsating flow (St >0) can be seen from Figure 8 by comparing the Nusellt number () value with the steady case (St =0).

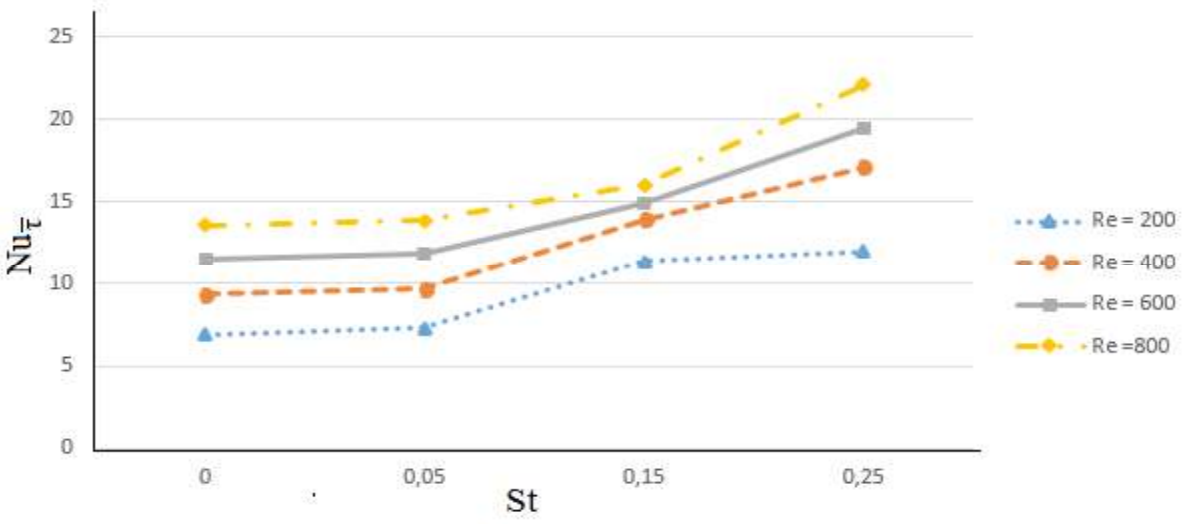

Figure. 8 Time-averaged Nusselt number (Nu) values at various strouhal numbers (St).

Enhancement of heat transfer is noteworthy for the Strouhal number (St) value of 0.05. At this value of the Strouhal number (St), an increase of heat transfer rate is around 6% and the Reynolds number does not cause big difference. This situation can also be observed from Figure 9. There are not a wide range differences between Nusselt numbers () based on strouhal numbers, St =0 and St=0.05. The effect of pulsating flow on heat transfer becomes more evident when the Strouhal number (St) is equal to 0.15. Heat transfer enhancement rate which goes upto 65% as comparing to the steady flow case and after that the effect of Reynolds number becomes important. As it is seen in Figure 9 enhancement heat transfer ratio is reduced when the Reynolds number is lower than 400. With the further increase of Strouhal number (St) the heat transfer enhancement ratio continues to increase. When the Strouhal number (St) is equal to 0.25 the Nusselt number () value increases up to 82%.

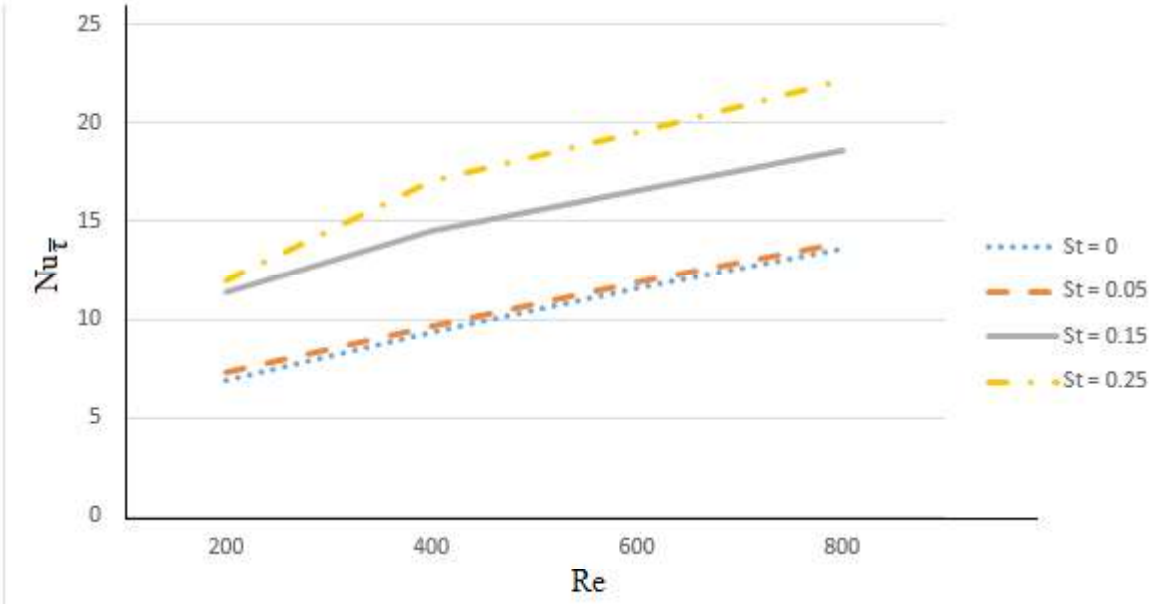

Figure 9. Time-averaged Nusselt number () values at various Reynolds numbers.

4. CONCLUSION

Pulsating flow and heat transfer through wavy channel numerically simulated for and . Variation of inlet dimensionless velocity (U) with respect to time causes that the Nusselt number () varies periodically. Time-averaged Nusselt numbers

(St) show that pulsating flow has positive contribution on the heat transfer rate for the geometry used in this study. The rate of heat transfer is strongly affected by the Strouhal number (St). Heat transfer enhancement is not significant and the effect of the Reynolds number is limited for the Strouhal number of St=0.05. This situation changes with increasing the Strouhal number (St); heat transfer enhancement gets better and the role of the Reynolds number becomes more dominant.

5. ACKNOWLEDGEMENT

The authors would like to express their appreciation to Ç.Ü. Scientific Research Project Department for their financal support (Project ID; FDK-2016-6952).

REFERENCES

[1] Guo, Z. and Sung, H.J. (1997). Analysis of the Nusselt number in pulsating pipe flow. International journal of heat and mass transfer, vol. 40, no. 10, pp. 2486-2489. 10.1016/S0017-9310(96)00317-1

[2] Chattopadhyay, H., Durst, F., and Ray, S. (2006). Analysis of heat transfer in simultaneously developing pulsating laminar flow in a pipe with constant wall temperature. International communications in heat and mass transfer, vol. 33, no. 4, pp. 475-481. 10.1016/j.icheatmasstransfer.2005.12.008

[3] Rahgoshay, M., Ranjbar, A.A., and Ramiar, A. (2012). Laminar pulsating flow of nanofluids in a circular tube with isothermal wall. International Communications in Heat and Mass Transfer, vol. 39, no. 3, pp. 463-469. 10.1016/j.icheatmasstransfer.2011.12.008

[4] Wang, X. and Zhang, N. (2005). Numerical analysis of heat transfer in pulsating turbulent flow in a pipe. International Journal of Heat and Mass Transfer, vol. 48, no. 19, pp. 3957-3970. 10.1016/j.ijheatmasstransfer.2005.04.011

[5] Mehta, B. and Khandekar, S. (2015). Local experimental heat transfer of single-phase pulsating laminar flow in a square mini-channel. International Journal of Thermal Sciences, vol. 91, pp. 157-166. 10.1016/j.ijthermalsci.2015.01.008

[6] Moon, J.W., Kim, S.Y., and Cho, H.H. (2005). Frequency-dependent heat transfer enhancement from rectangular heated block array in a pulsating channel flow. International journal of heat and mass transfer, vol. 48, no. 23, pp. 4904-4913. 10.1016/j.ijheatmasstransfer.2005.06.006

[7] Ji, T.H., Kim, S.Y., and Hyun, J.M. (2008). Experiments on heat transfer enhancement from a heated square cylinder in a pulsating channel flow. International Journal of Heat and Mass Transfer, vol. 51, no. 5, pp. 1130-1138. 10.1016/j.ijheatmasstransfer.2007.04.015

[8] Kim, S.Y., Kang, B.H., and Jaluria, Y. (1998). Thermal interaction between isolated heated electronic components in pulsating channel flow. Numerical Heat Transfer, Part A Applications, vol. 34, no. 1, pp. 1-21. Doi 10.1080/10407789808913974

[9] Jin, D., Lee, Y., and Lee, D.-Y. (2007). Effects of the pulsating flow agitation on the heat transfer in a triangular grooved channel. International journal of heat and mass transfer, vol. 50, no. 15, pp. 3062-3071. 10.1016/j.ijheatmasstransfer.2006.12.001

[10] Nandi, T.K. and Chattopadhyay, H. (2013). Numerical investigations of simultaneously developing flow in wavy microchannels under pulsating inlet flow condition. International Communications in Heat and Mass Transfer, vol. 47, pp. 27-31. 10.1016/j.icheatmasstransfer.2013.06.008

[11] Akdag, U., Akcay, S., and Demiral, D. (2014). Heat transfer enhancement with laminar pulsating nanofluid flow in a wavy channel. International Communications in Heat and Mass Transfer, vol. 59, pp. 17-23.

[12] Jafari, M., Farhadi, M., and Sedighi, K. (2014). Heat transfer enhancement in a corrugated channel using oscillating flow and nanoparticles: an LBM approach. Numerical Heat Transfer, Part A: Applications, vol. 65, no. 6, pp. 601-626. 10.1080/10407782.2013.836023

[13] Alawadhi, E.M. and Bourisli, R.I. (2009). The role of periodic vortex shedding in heat transfer enhancement for transient pulsatile flow inside wavy channels. Int. Journal of Natural Sciences and Engineering, vol. 1, no. 2, pp. 79-85.

[14] Chattopadhyay, H., Durst, F., and Ray, S. (2006). Analysis of heat transfer in simultaneously developing pulsating laminar flow in a pipe with constant wall temperature. International communications in heat and mass transfer, vol. 33, no. 4, pp. 475-481. 10.1016/j.icheatmasstransfer.2005.12.008

[15] Wang, C.-C. and Chen, C.-K. (2002). Forced convection in a wavy-wall channel. International Journal of Heat and Mass Transfer, vol. 45, no. 12, pp. 2587-2595.